Journal of Non-Newtonian Fluid Mechanics 244 (2017) 57–74

Contents lists available at ScienceDirect

Journal of Non-Newtonian Fluid Mechanics

journal homepage: www.elsevier.com/locate/jnnfm

Stability of shear banded flow for a viscoelastic constitutive model with thixotropic yield stress behavior

Yuriko Renardy*, Michael Renardy

Department of Mathematics, 460 McBryde Hall, 225 Stanger Street, Virginia Tech, Blacksburg, VA 24061-0123, USA

ARTICLE INFO

Article history:
Received 19 October 2016
Accepted 12 April 2017
Available online 18 April 2017

MSC:
74H55
76A05
76E05

Keywords:
Shear banding
Yield stress fluid
Flow stability
PEC model

ABSTRACT

A viscoelastic constitutive model which combines the partially extending strand convection model and a Newtonian solvent is used in the regime of large relaxation time. Prior work on one dimensional time-dependent solutions at prescribed shear stress predicts some of the features expected of thixotropic yield stress fluids, such as delayed yielding. In this paper, we present the linear stability analysis of two-dimensional plane Couette flow, for parameter regimes that support a two-layer arrangement consisting of an unyielded layer and a yielded layer. Asymptotic analysis and computational techniques are applied. We find that the one layer yielded flow can have bulk instabilities which also emerge in the two-layer flow. Bulk instabilities in the yielded phase appear not to have been observed in prior literature. For some parameters, an interfacial mode is unstable and is driven by the normal stress difference across the interface. The yielded zone has the higher first normal stress difference, as for the well-studied Johnson–Segalman model. In order to assess the importance of the sign of the first normal stress difference at the interface, we specifically design a modification to the model to reverse the sign. It is found that instabilities still occur.

© 2017 Elsevier B.V. All rights reserved.

1. Introduction

Shear banding is the coexistence of high shear rate (“yielded”) and low shear rate (“unyielded”) zones at the same shear stress, and occurs in many complex fluids such as wormlike micellar solutions, pastes and suspensions [1–6]. In this work, we are interested in instabilities of shear banded flows. We find that these arise both from the bulk and at the interface between the two zones.

In the limit of a long relaxation time, the PECN model (partially extending strand convection model and Newtonian solvent) predicts certain characteristic behaviors of thixotropic yield stress fluids [7], allowing a precise mathematical expression of the idea that yield stress behavior is really a limit of extremely long relaxation time [8]. The yielding and unyielding hehavior of the model under an imposed constant stress has been analyzed in prior work [7], and we briefly summarize the results. Specifically, the model equations contain a small paramter ϵ, which physically corresponds to a ratio of retardation time to relaxation time; in our nondimensionalization below, time is scaled with the retardation time. If we formally set $\epsilon = 0$, the PECN model reduces to a nonlinear elastic model, and this phase describes the initial evolution from equilibrium when a stress is suddenly imposed. The elastic shear stress assumes a maximum at a certain value of shear deformation and then decreases to zero as the shear is increased further.

With small but non-zero ϵ, the steady shear response is non-monotone, with a stress maximum of order 1 at a shear rate of order ϵ, and a stress minimum of order $\epsilon^{1/4}$ at a shear rate of order $\epsilon^{1/4}$. For nonzero ϵ, there is no “true” yield stress; the shear rate in the “unyielded” regime is nonzero but small, of order ϵ. Thus, simply setting $\epsilon = 0$ in the governing equations gives only an incomplete picture of the dynamics, because different asymptotic regimes that depend on ϵ arise when long times and/or large deformations arise. These different regimes are considered in detail in [7]. One of the results of the interplay of these dynamic regimes is delayed yielding: The value of the stress maximum in steady shear flow is lower (by a factor $\sqrt{2}$) than the elastic shear stress maximum. If the imposed shear stress is higher than the elastic maximum, yielding will happen immediately, but if the imposed stress lies between the steady and elastic maxima, yielding will happen eventually, on a long time scale of order $1/\epsilon$. In summary, the small ϵ asymptotic analysis shows that flow is induced if either the shear stress exceeds the elastic stress maximum (immediate yielding), or the maximum on the steady flow curve (delayed yielding). Once flow begins, the yield stress is lowered, i.e. there is yield stress hysteresis.

If the shear stress is suddenly removed in an established yielded flow, the motion will cease quickly, but the viscosity will

---

* Corresponding author.
E-mail address: renardy@vt.edu (Y. Renardy).

http://dx.doi.org/10.1016/j.jnnfm.2017.04.005
0377-0257/© 2017 Elsevier B.V. All rights reserved.

return to its equilibrium value (which is of order $1/\epsilon$) only over a timescale of order $1/\epsilon$, i.e. we observe thixotropic behavior. This is documented in [9].

In a shear rate controlled experiment, there is no stable homogeneous steady flow if the imposed shear rate falls into the interval where the steady response curve is decreasing. However, there are shear banded solutions, where two or more layers are formed, and in each layer the shear rate is on an increasing part of the steady flow curve. The shear stress is continuous across the boundary between layers, but the normal stress is not.

Parallel flows consisting of layers of two different viscoelastic fluids may have interfacial instabilities driven by a normal stress jump at the interface. Such instabilities were first found in the flow of two upper convected Maxwell fluids by Renardy [10] and Chen [11]. A shear banded flow, resulting from a non-monotone constitutive curve is analogous to this; although the two layers are the same fluid, they have different shear rates and normal stresses, and the interface can be treated as a material surface. Renardy [12] investigated the shear-banded flow of a Johnson–Segalman fluid and found interfacial instabilities driven by a normal stress jump. Her analysis was later expanded, most notably by a study of the long wave limit and by the inclusion of stress diffusion at the interface [13–15]. Even earlier, McLeish [16] found a normal-stress driven interfacial instability in shear-banded flow of a Doi-Edwards fluid. Rather than a full linear stabiity analysis, he used a simplified set of equations which was intended to capture the essential physics of long-wave instabilities.

There is much work based on the Johnson–Segalman model [13–15,17–19]. On the other hand, there are other established models that display non-monotone constitutive behavior and shear banded flows; for example, PECN is a Newtonian solvent model combined with a “partially extending strand convection” model, originally introduced by Larson [20] for entangled polymer melts. The Vasquez-Cook-McKinley (VCM) model is a refinement of this, which has had success in modeling the behavior of wormlike micellar solutions [21].

Fluids which show shear banding include wormlike micelles, some polymers and soft glassy materials [3]. Instabilities in shear banded flows have been observed in wormlike micelles. Experiments are typically done in curved geometries, where, aside from the interfacial instability there is also the possibility of a viscoelastic Taylor instability. It is believed that the Taylor instability is the dominant mechanism in most of the experimental observations [3]. There are, however, some experiments showing instabilities which have been attributed to interfacial mechanisms; we cite in particular [22] and [23]. Both first and second normal stress jumps can cause interfacial instabilities. The instability observed in [22] leads to interface oscillations in the spanwise direction, as would be expected from a second normal stress effect. In [22], the authors link the experimental observations to an analysis of the Johnson–Segalman model [18], which shows that although streamwise waves have a larger linear growth rate, nonlinear interactions ultimately favor spanwise perturbations. However, Fig. 2 in [22] shows no evidence of transient growth of any streamwise waves. The experiments of [23] show streamwise corrugations of the interface as would result from an instability driven by a jump in the first normal stress difference. We note that, unlike the Johnson–Segalman model, neither the PEC nor the VCM model has a second normal stress difference.

The analysis presented below shows that shear banded flows of the PECN model have instabilities. We are not aware of prior studies of the PECN model per se. However, [24] studied the stability of diffusive interfaces for the VCM model, and interfacial instabilities were found.

Our analysis shows that actually there are instabilities in the yielded phase even when there is no interface. Where they are

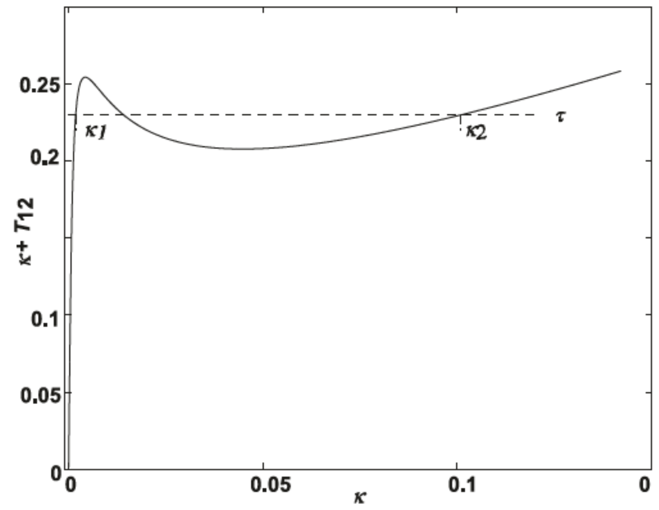

Fig. 1. Total shear stress $\kappa(s) + T_{12}(s)$ as a function of shear rate $\kappa(s)$. The dashed line denotes the prescribed total shear stress τ, and intersects the increasing parts of the curve at κ_1 and κ_2. The specific parameters for the PECN model are $\alpha = -1$, $\epsilon = 0.001$.

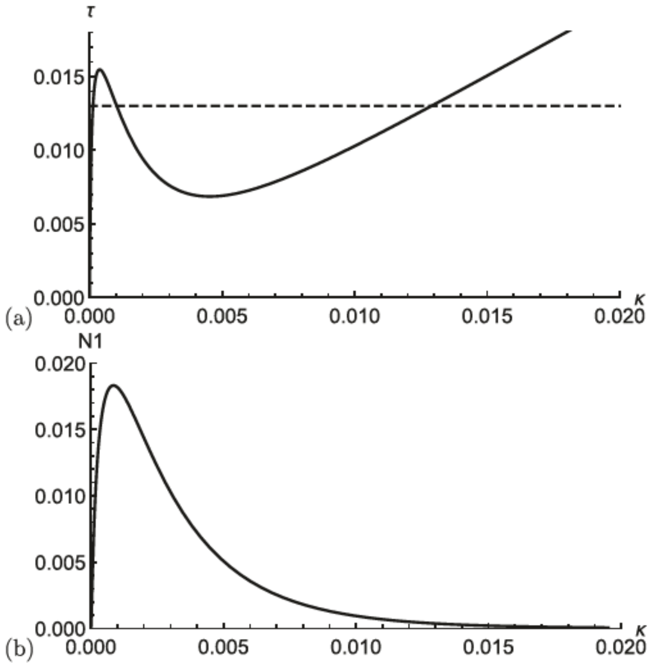

Fig. 2. Altered PEC model with $\psi(s) = \exp(-s)$, $\alpha = -2.8$, $\epsilon = 0.001$. (a) Steady state solutions for total shear stress τ versus shear rate κ $(= U'(y))$. (b) Steady state solutions for the first normal stress difference N_1 versus κ.

present, these bulk instabilities, rather than interfacial instabilities, turn out to be the dominant mechanism of instability in shear-banded flows. The modes responsible for these bulk instabilities bifurcate from the (stable) continuous spectrum at some wave number, then become unstable over an interval of wave numbers, and in some cases eventually restabilize and merge back into the continuous spectrum. Such modes do not seem to have been observed in prior literature. The only results on single-phase instabilities in viscoelastic shear flow without streamline curvature that we are aware of are those of [25,26]; these papers, however, studied Poiseuille rather than Couette flow.

We also find unstable interfacial modes. We note that, for both the Johnson–Segalman and PEC-based models, the normal stress difference in the yielded phase is larger than in the unyielded

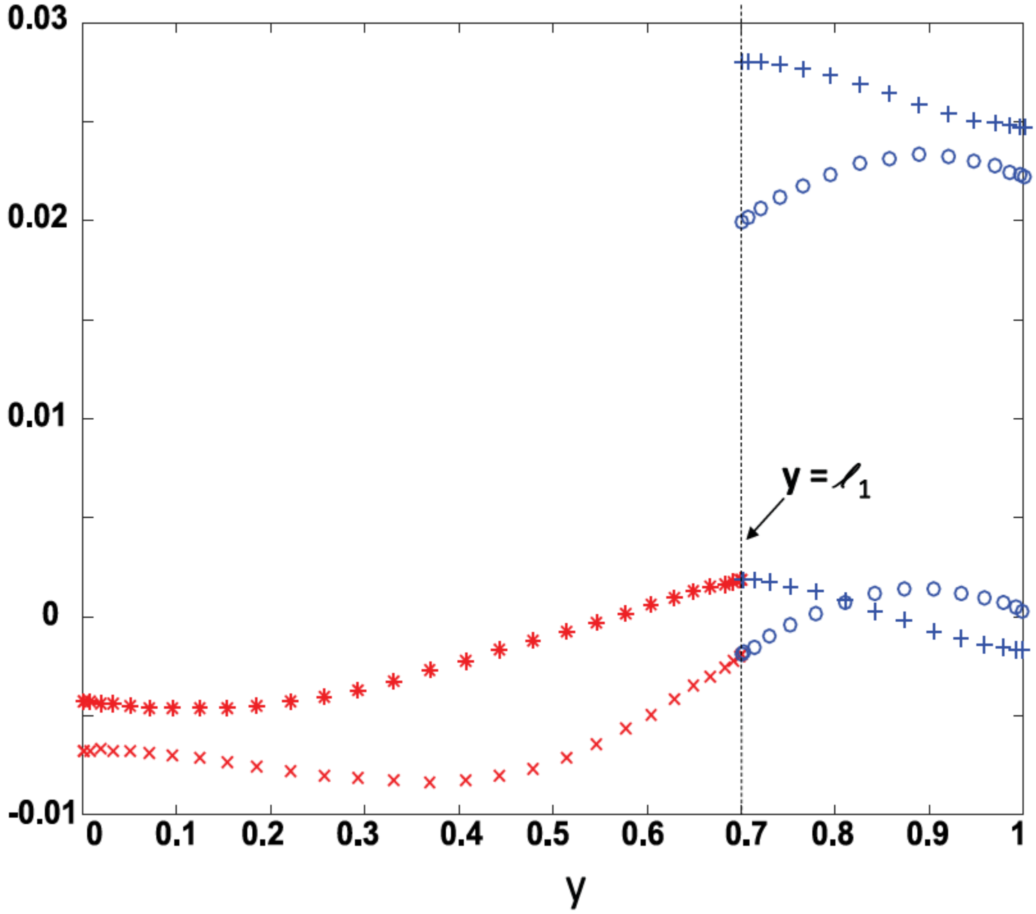

Fig. 3. The real (*) and imaginary (x) parts of the pressure eigenfunction are plotted in fluid 1, and (real +; imaginary o) in fluid 2. This illustrates the pressure field of a spurious mode, and shows oscillations in the yielded phase between every discretized point.

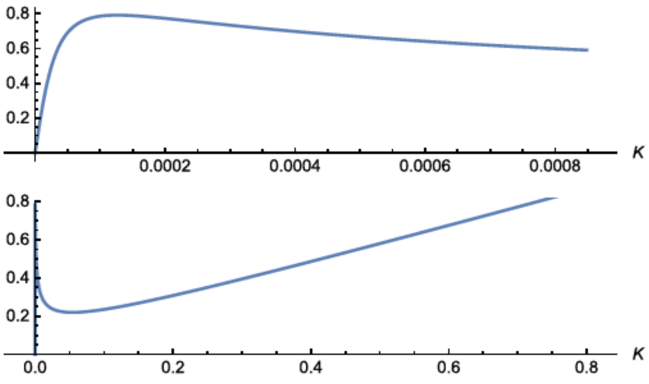

Fig. 4. Shear rate κ vs applied shear stress τ, $\epsilon = 0.001$, $\alpha = -2.8$.

phase. The experimental data for wormlike micelles reported in [27] are consistent with this. Since the normal stress jump is driving the instability, this is an important feature that both models have in common, and it is a natural question whether this is important for generating interfacial instability. We note, however, that in the flow of two-layer upper convected Maxwell fluids the question of, "Which sign of the normal stress jump leads to instability?" does not appear to have a straightforward answer; for short wave disturbances, a higher normal stress difference in the fluid with lower viscosity is actually stabilizing [10]. In contrast, the Johnson–Segalman and PEC models show instability with a higher normal stress in the yielded (low viscosity) phase. This motivates us to pose a more strongly shear thinning model where the yielded phase has the lower normal stress. We introduce this model below in more detail. It is natural to ask whether interfacial instabilities disappear when the normal stress jump is reversed. We find that this is not the case. The VCM model also allows for the possibility that the normal stress is lower in the yielded phase [27,28]; the data to which the model is fitted, however, do not show this. Interfacial stability for this model was studied [24] for a specific set of parameters fitted to experiments. For these specific parameters, the model does have a lower normal stress differences in the yielded phase, but this particular feature is in disagreement with

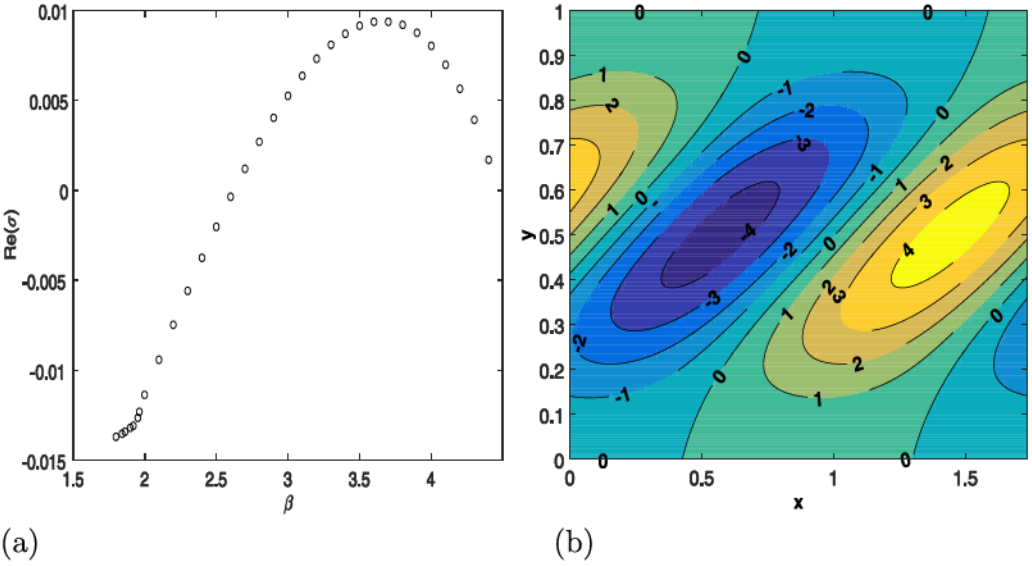

(a) (b)

Fig. 5. (a) Growth rate of unstable mode for yielded flow, $\alpha = -1$, $\kappa = 0.08397$. (b) Perturbation stream function for $\beta = 3.6$. Contour values are in units of 10^{-5}.

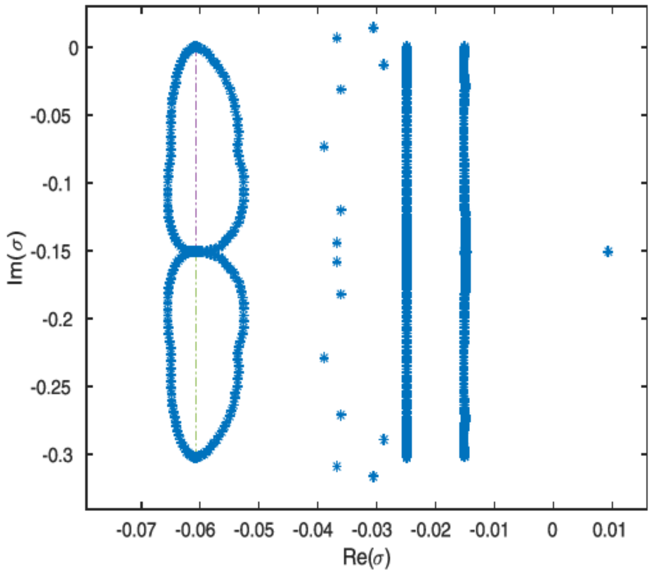

Fig. 6. Computed spectrum for yielded flow, $\alpha = -1$, $\kappa = 0.08397$, $\beta = 3.6$.

the data. The model discussed below has a much more drastic decrease in the first normal stress difference than what is reported in [27] for the VCM model.

Our analysis does not include stress diffusion. Diffusive effects favor a particular stress level for the shear banding transition, while without diffusion any stress between the maximum and minimum value of the nonmonotone curve can lead to a shear banded flow. However, there is considerable uncertainty about the magnitude and precise form of diffusive terms. Strictly speaking, the diffusion requires another constitutive law on which little is known. It has been shown that the form of stress diffusion does affect the location of the shear banding transition [29]. Moreover, diffusive effects are small, and there is a separation in time scales between the formation of a shear banded flow and the migration of the transition to its ultimate location [30]. Instabilities therefore have time to grow before the ultimate location is reached, and the stability analysis without diffusion is relevant for predicting them.

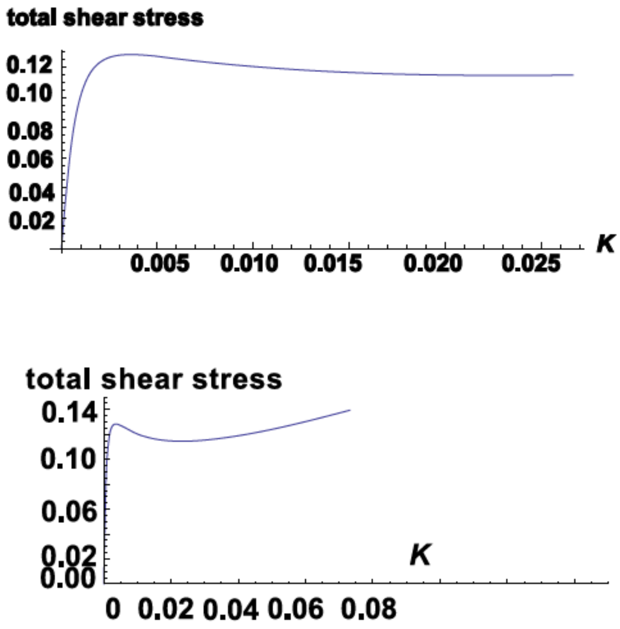

Fig. 7. Steady shear stress versus shear rate κ. $\alpha = 5$, $\epsilon = 0.0001$. The upper plot magnifies for small κ.

2. Governing equations and steady shear flow

We consider flow in the region between two parallel horizontal plates, of which the lower plate is stationary and the upper plate is moving. The governing equations for the PEC model are presented in the form given in [7].

Let $\mathbf{v}^*$ denote the velocity, p^* the pressure, ρ the density, η the constant solvent viscosity, λ the relaxation time, (x^*, y^*) the spatial coordinates, $\mathbf{C}$ the conformation tensor, $\mathbf{T}^*$ the extra stress tensor, L^* the plate separation, l_1^* the undisturbed lower fluid depth, U_p^* the upper plate speed in the x^*-direction. The governing equations for momentum conservation, incompressibility, and constitutive law are:

$$\rho \frac{D\mathbf{v}^*}{Dt^*} = \nabla^* \cdot (-p^*\mathbf{I} + \mathbf{S}^* + \mathbf{T}^*), \quad \nabla^* \cdot \mathbf{v}^* = 0, \tag{1}$$

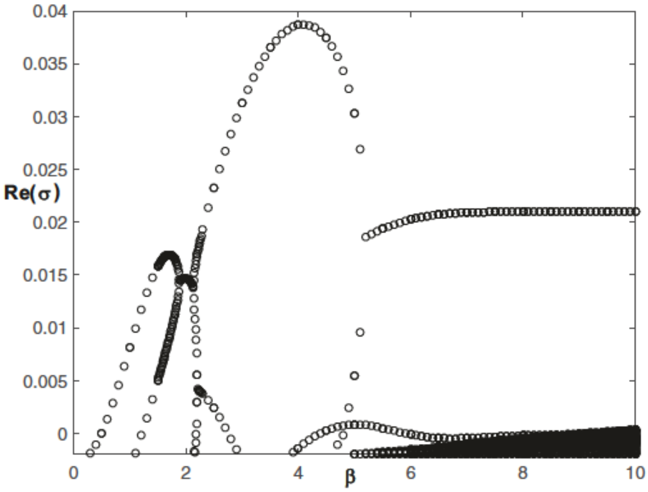

Fig. 8. Unstable modes for $\alpha = 5$, $\epsilon = 0.0001$, $\tau = 0.12$, $\kappa = 0.0422$.

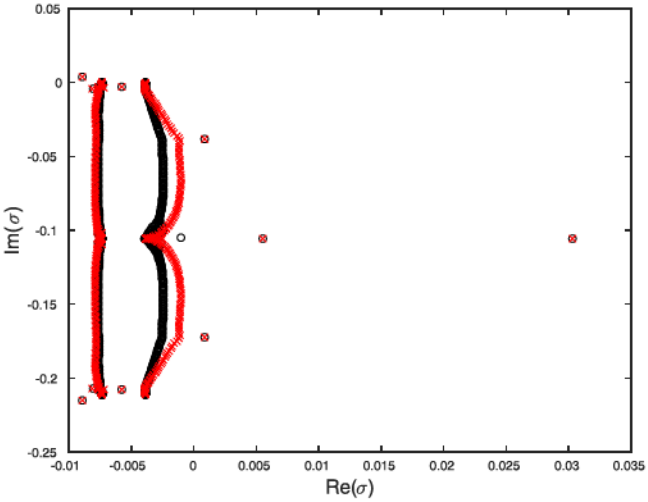

Fig. 9. Computed spectrum for $\beta = 5$, other parameters corresponding to Fig. 8. Comparison of $N = 100$ and $N = 200$.

$$\mathbf{C}^{\nabla *} + \frac{1}{\lambda}(\phi(\operatorname{tr}\mathbf{C})\mathbf{C} - \chi(\operatorname{tr}\mathbf{C})\mathbf{I}) = \mathbf{0}, \qquad \mathbf{T}^* = \psi^*(\operatorname{tr}\mathbf{C})\mathbf{C}, \tag{2}$$

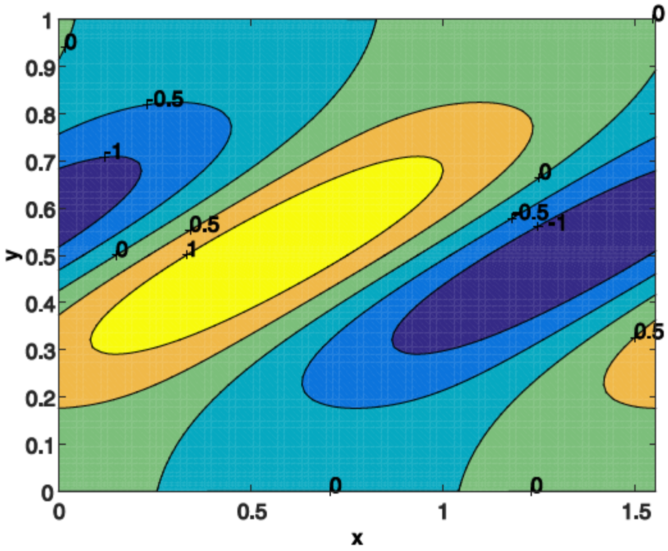

Fig. 11. Stream function contour plot for the most unstable mode at $\beta = 4$, parameters corresponding to Fig. 8. Contour values are in units of 10^{-5}.

where the PEC model functions are

$$\psi^*(s) = \frac{k_1}{s+\alpha}, \quad s = \operatorname{tr}\mathbf{C}, \qquad \phi(s) = \chi(s) = s + \alpha. \tag{3}$$

$\mathbf{C}^{\nabla *}$ denotes the upper convected derivative, $\mathbf{C}^{\nabla *} \equiv \frac{D\mathbf{C}}{Dt^*} - (\nabla^*\mathbf{v}^*)\mathbf{C} - \mathbf{C}(\nabla^*\mathbf{v}^*)^T$, where $\frac{D}{Dt^*} = \frac{\partial}{\partial t^*} + \mathbf{v}^* \cdot \nabla^*$. The Newtonian contribution to the stress tensor is

$$\mathbf{S}^* = \eta(\nabla^*\mathbf{v}^* + (\nabla^*\mathbf{v}^*)^T), \quad (\nabla^*\mathbf{v}^*)_{ij} = \frac{d\mathbf{v}_i^*}{dx_j^*}. \tag{4}$$

The microstructure is fully relaxed when $\mathbf{C} = \mathbf{I}$ (hence $s = 3$), and only states with $s \geq 3$ are physically reachable and relevant. The model functions are defined if $\alpha > -3$. Let τ^* denote the applied shear stress. The retardation time is defined by $\bar{t} = \eta / k_1$.

We shall replace the dimensional variables, denoted by asterisks above, with dimensionless quantities. To this end, time is scaled with the retardation time, length with the plate separation, and stress and pressure with k_1. The ratio of retardation to relaxation time is

$$\epsilon = \frac{\eta}{k_1 \lambda}. \tag{5}$$

The dimensionless upper plate speed is $U_p = U_p^* \bar{t} / L^*$.

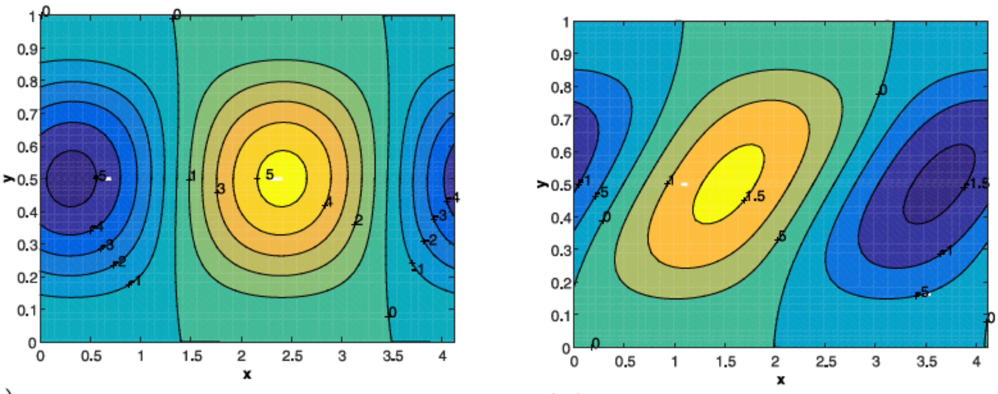

(a) (b)

Fig. 10. Stream function contour plots of unstable modes for $\beta = 1.5$, other parameters corresponding to Fig. 8. Contour values are in units of 10^{-5}. Plot (a) shows the mode with higher growth rate.

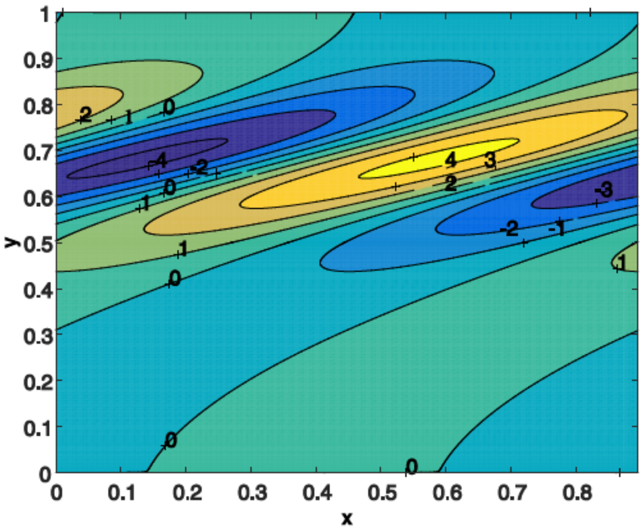

Fig. 12. Stream function contour plot for the most unstable mode at $\beta = 7$, parameters corresponding to Fig. 8. Contour values are in units of 10^{-6}. There is a pair of unstable modes, the second mode is symmetric to the one shown here.

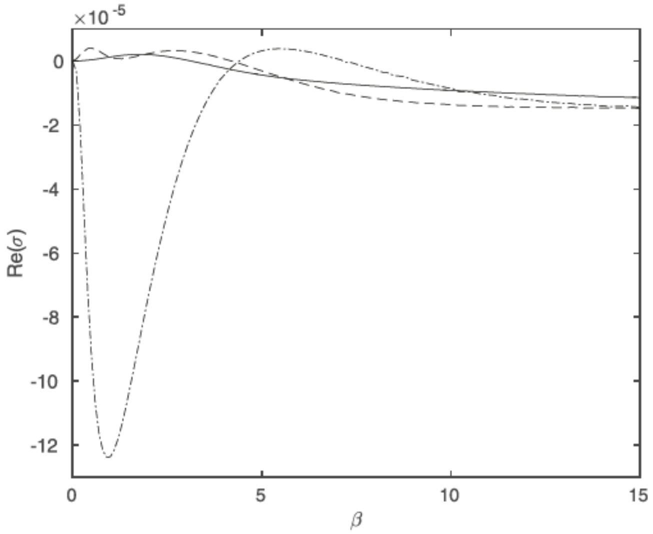

Fig. 13. Growth rate of unstable modes for $\epsilon = 0.001$, $\alpha = -2.8$, $\tau = 0.65$. Solid curve: $l_1 = 0.2$, dashed: $l_1 = 0.5$, dash-dotted: $l_1 = 0.7$.

In dimensionless form, the governing equations are

$$Re\frac{D\mathbf{v}}{Dt} = \nabla\cdot(-p\mathbf{I} + \mathbf{S} + \mathbf{T}), \tag{6}$$

$$\nabla\cdot\mathbf{v} = 0, \tag{7}$$

$$\mathbf{C}^{\nabla} + \epsilon(\phi(\operatorname{tr}\mathbf{C})\mathbf{C} - \chi(\operatorname{tr}\mathbf{C})\mathbf{I}) = \mathbf{0}, \tag{8}$$

where $\mathbf{C}^{\nabla} \equiv \frac{D\mathbf{C}}{Dt} - (\nabla\mathbf{v})\mathbf{C} - \mathbf{C}(\nabla\mathbf{v})^T$, $\frac{D}{Dt} = \frac{\partial}{\partial t} + \mathbf{v}\cdot\nabla$, $\mathbf{S} = \nabla\mathbf{v} + (\nabla\mathbf{v})^T$, $\nabla\mathbf{v} = \frac{dv_i}{dx_j}$, and the elastic stress tensor is

$$\mathbf{T} = \psi(s)\mathbf{C}, \quad \psi(s) = \frac{1}{s+\alpha}. \tag{9}$$

The Reynolds number is $Re = L^{*2}\rho k_1/\eta^2$, and $We = U_p/\epsilon$ has the role of a Weissenberg number. The focus of this paper will be on the case where Re and ϵ are small.

Apart from ϵ, the only dimensionless model parameter is α. More physically meaningful combinations of these parameters are the ratio of yielded to unyielded (zero shear rate) viscosity, which is $\epsilon(3+\alpha)^2$, and the ratio of the yield stress in fast yielding to the instantaneous elastic modulus, which is $\sqrt{3+\alpha}/2$. Hence a large value of α corresponds to a high yield stress, while α close to -3 corresponds to a low yield stress. Fits to wormlike micelles yield positive values of α, which are typically on the order of 1–10, the ratio of yielded to unyielded viscosity is on the order of 10^{-3}–10^{-2}. On the other hand, soft glassy materials typically have a low yield stress ($\alpha < -2.5$) and ϵ is extremely small (see [9] for some fits of the model to experimental data).

Our "base flow" is a steady parallel flow in the x-direction, with a velocity that depends only on the vertical coordinate y and a shear stress τ is that is constant across the flow region. We begin by showing the single shear rate case, before defining the base flow with two shear rates more precisely.

In parallel shear flow, the components of the conformation tensor satisfy

$$\begin{aligned}
\dot{C}_{11} &= 2(\tau - \psi(s)C_{12})C_{12} + \epsilon(\chi(s) - \phi(s)C_{11}),\\
\dot{C}_{12} &= \tau - \psi(s)C_{12} - \epsilon\phi(s)C_{12},\\
C_{13} &= C_{23} = 0, \qquad C_{22} = C_{33} = 1.
\end{aligned} \tag{10}$$

The shear rate is denoted

$$\kappa = \partial u/\partial y = \tau - \psi(s)C_{12},$$

and the trace of the conformation tensor is

$$s = C_{11} + 2.$$

A steady homogeneous shear flow solution is given by the velocity $\mathbf{v} = (\kappa y, 0, 0)$, $0 \le y \le 1$, at the total shear stress τ. The conformation tensor satisfies

$$C_{11} = 1 + \frac{2\kappa(s)^2}{\epsilon^2\phi^2(s)}, \quad C_{12} = \frac{\kappa(s)}{\epsilon\phi(s)} = C_{21}, \tag{11}$$

The elastic contribution to the shear stress, T_{12}, shear rate κ, and normal stress difference satisfy:

$$T_{12} = \frac{1}{s+\alpha}\sqrt{\frac{s-3}{2}}, \tag{12}$$

$$\frac{\kappa}{\epsilon} = (s+\alpha)\sqrt{\frac{s-3}{2}}, \tag{13}$$

$$N_1 = T_{11} - T_{22} = \frac{s-3}{s+\alpha}. \tag{14}$$

Fig. 1 illustrates the total shear stress $\tau = T_{12} + \kappa$ as a function of shear rate for steady solutions. The solutions on the decreasing part of the curve are unstable. Moreover, this gives the range of τ that forms shear banded flows with two different shear rates. The base flow for two-layer parallel shear flow is given by $\mathbf{v}_B = (U(y), 0, 0)$ where

$$U(y) = \begin{cases} \kappa_1 y & 0 < y < l_1 \\ \kappa_2(y-1) + U_p. & l_1 < y < 1 \end{cases} \tag{15}$$

The continuity of velocity at $y = l_1$ gives $\kappa_1 l_1 = \kappa_2(l_1 - 1) + U_p$, which determines U_p once the shear rates are determined. The shear rates are determined from the continuity of the total shear stress. The base conformation tensor is given by (11) in each fluid. The lower layer is denoted by subscript $B1$, where $s = s_{B1}$ for the base flow (15) that produces the shear rate $\kappa_1 = \kappa(s_{B1})$. The upper layer is at the shear rate $\kappa_2 = \kappa(s_{B2})$, which defines the value of s_{B2}. These are shown in Fig. 1 where the dashed line guides the eye at a constant τ, to its intersections with the curve on the increasing branches. Physically, the plate speed controls the development of shear banded flows by playing the role of the average shear rate.

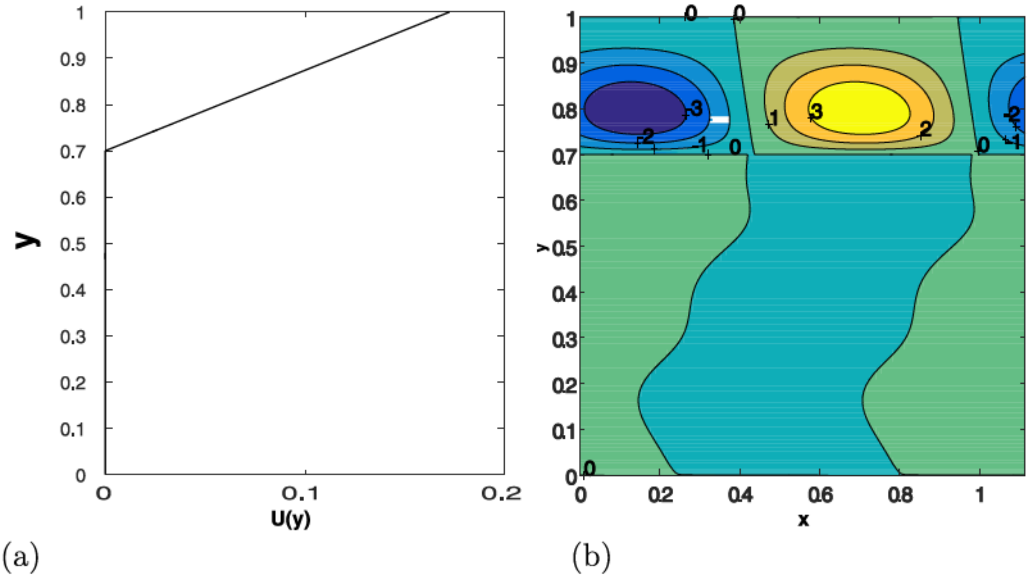

(a) (b)

Fig. 14. Stream function of interfacial mode for Fig. 13 at $l_1 = 0.7$. (a) base flow profile, (b) $\beta = 5.6$. Contour values in units of 10^{-5}.

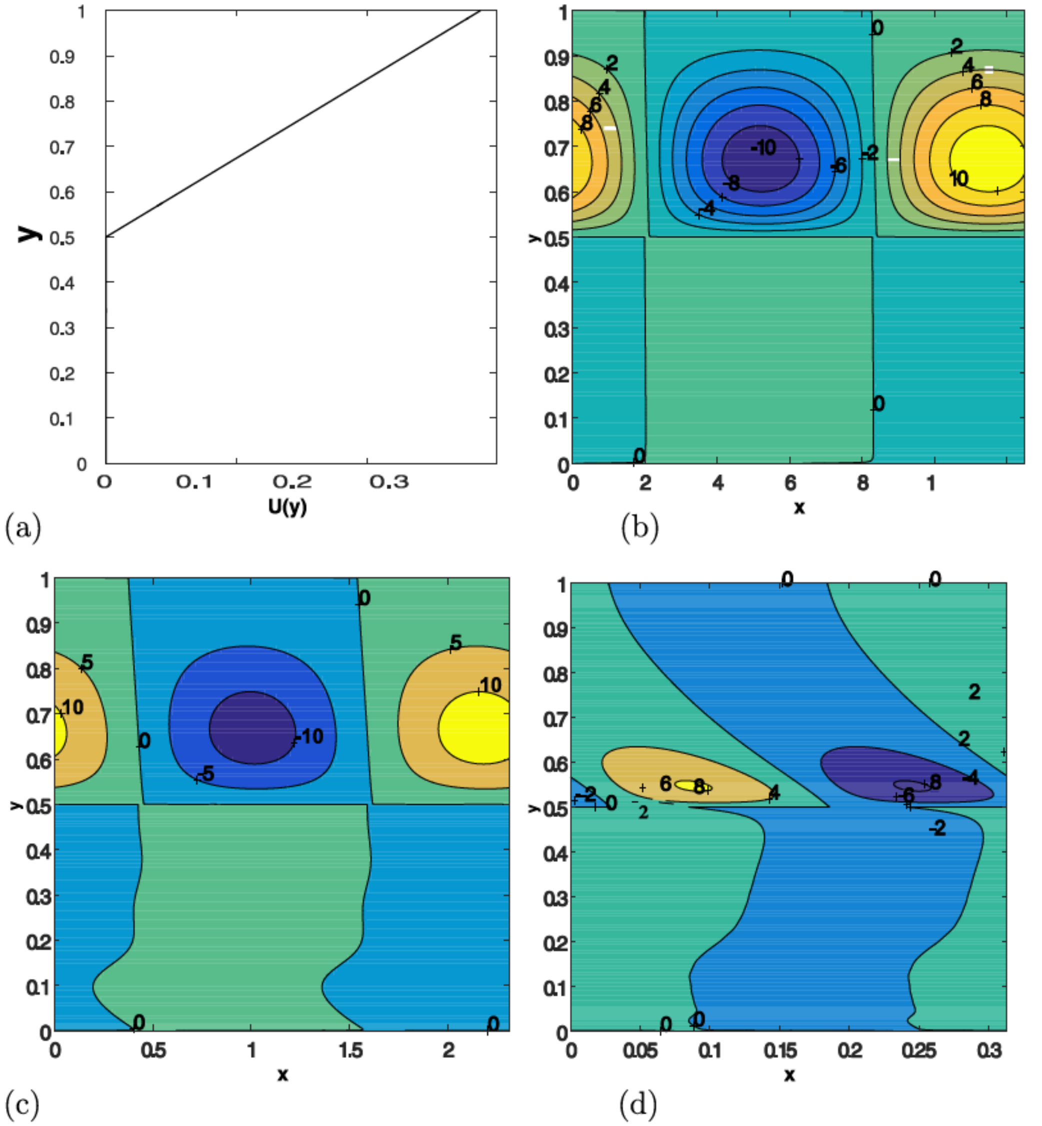

(a) (b) (c) (d)

Fig. 15. Stream function of interfacial mode for Fig. 13 at $l_1 = 0.5$. Contour values in units of 10^{-5}. (a) base flow profile, (b) $\beta = 0.5$, (c) $\beta = 2.7$, (d) $\beta = 20$.

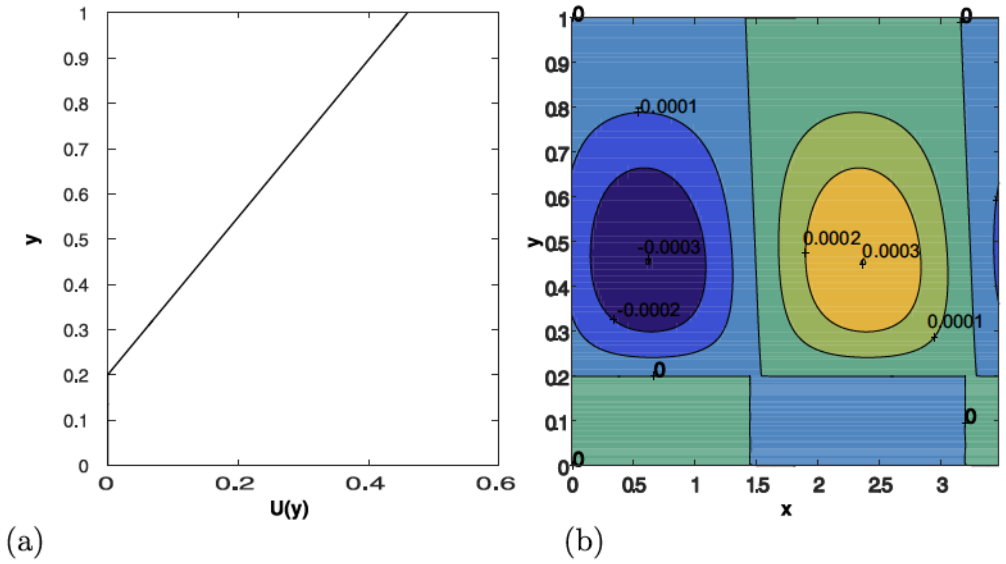

(a) (b)

Fig. 16. Stream function of interfacial mode for Fig. 13 at $l_1 = 0.2$. (a) base flow profile, (b) $\beta = 1.8$.

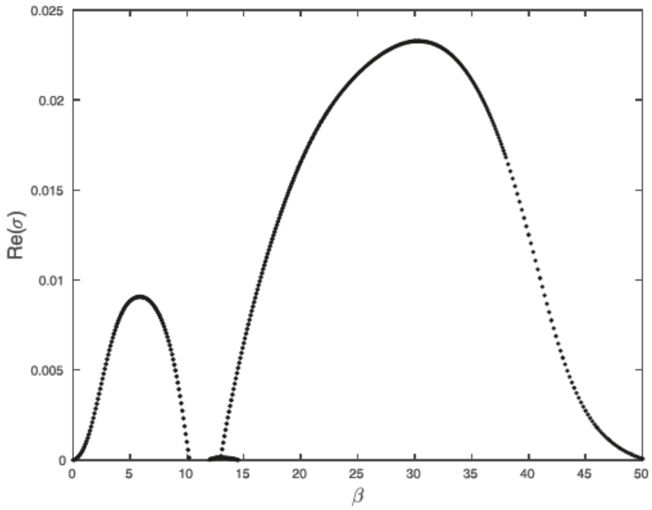

Fig. 17. Growth rate of unstable modes for $\alpha = -1$, $\tau = 0.22$, $l_1 = 0.9$.

The first normal stress difference is $N_1 = \frac{s_B - 3}{s_B + \alpha}$, and we note from (13) that the N_1 and the shear rate are both monotone functions of s. Hence, the normal stress difference increases with shear rate. In particular, the high shear rate region in a shear banded flow has the higher normal stress difference.

Altered PEC model with lower N_1 *at higher shear rates*

To investigate an alternative model where the high shear rate region has the lower N_1, we modify the PEC model by keeping $\phi(s) = \chi(s) = s + \alpha$, but setting

$$\psi(s) = e^{-s}. \tag{16}$$

The base flow remains the same as (15), with $\kappa = U'(y)$. The formula (11) for the base conformation tensor stays the same. The total shear stress is now given by

$$\tau = T_{B12} + S_{B12} = \kappa\left(\frac{e^{-s_B}}{\epsilon(s_B + \alpha)} + 1\right). \tag{17}$$

Fig. 2(a) shows $\tau(s)$ versus $\kappa(s)$ and displays the non-monotonicity that leads to shear banding, and we see this also in Fig. 1. The difference is that in Fig. 2(a), the graph approaches a line $\tau \sim \kappa$ for large s, irrespective of ϵ or α, because of the exponential decay of $\psi(s)$. The two values of shear rates which satisfy continuity of shear stress are found from drawing the dashed horizontal line, as before. Fig. 2(b) shows the normal stress difference, which is now lower in the high shear rate phase. For lack of a more established name, we introduce this model as the "altered" PEC model.

3. Linear stability of shear banded PECN flow

We consider small two-dimensional perturbations of shear banded flow (15) and linearize the governing equations. The perturbations are denoted by lower case variables, e.g., (u, v, p). The interface position is perturbed by $h(x, t)$. We separate variables and seek solutions proportional to $\exp(\sigma t + i\beta x)$. This results in the following linearized system. The governing equations are the momentum equations,

$$\begin{aligned} Re\ (\sigma + Ui\beta)u + Re\ v\ U' &= -i\beta p - \beta^2 u + u'' + i\beta T_{11} + T_{12}', \\ Re\ (\sigma + Ui\beta)v &= -p' - \beta^2 v + v'' + i\beta T_{12} + T_{22}', \end{aligned} \tag{18}$$

where the perturbed extra stress components are

$$\begin{aligned} T_{11} &= \psi(s_B)C_{11} + C_{11B}\psi'(s_B)(C_{11} + C_{22}), \\ T_{12} &= \psi(s_B)C_{12} + C_{12B}\psi'(s_B)(C_{11} + C_{22}), \\ T_{22} &= \psi(s_B)C_{22} + C_{22B}\psi'(s_B)(C_{11} + C_{22}). \end{aligned} \tag{19}$$

The incompressibility condition is,

$$i\beta u + v' = 0, \tag{20}$$

and the constitutive equations are

$$\begin{aligned} &(\sigma + i\beta U(y) + \epsilon(s_B + \alpha) + \epsilon(C_{B11} - 1))C_{11} \\ &+\epsilon C_{22}(C_{B11} - 1) - (2i\beta C_{B11}u + 2C_{B12}u' + 2U'C_{12}) = 0, \\ &(\sigma + i\beta U(y) + \epsilon(s_B + \alpha))C_{12} + \epsilon(C_{11} + C_{22})C_{B12} \\ &-(i\beta C_{B11}v + C_{B12}v' + C_{B12}i\beta u + u' + U'C_{22}) = 0, \\ &(\sigma + i\beta U(y) + \epsilon(s_B + \alpha))C_{22} - (2C_{B12}i\beta v + 2v') = 0. \end{aligned} \tag{21}$$

Let $[[\cdot]]$ denote the jump of a quantity across the interface linearized at $y = l_1$. In the base flow, the velocity gradient and first normal stress difference both jump across the interface. The linearized interface conditions imposed at $y = l_1$ are: continuity of

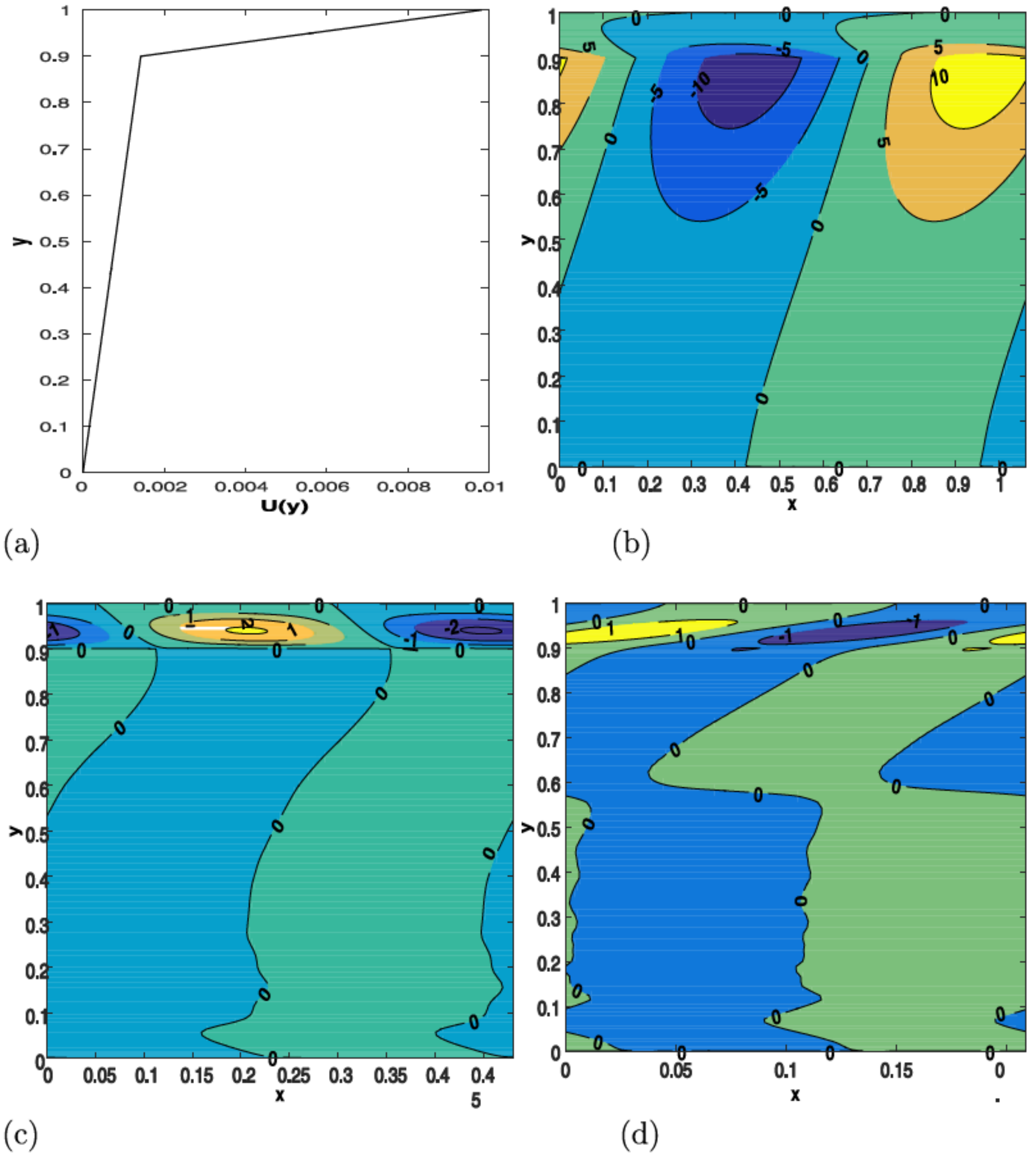

(a) (b) (c) (d)

Fig. 18. Stream functions of unstable modes for Fig. 17. (a) base flow profile, (b) $\beta = 5.9$, (c) $\beta = 13$, (d) $\beta = 30$. Contour values in units of 10^{-6}.

velocity,

$$\llbracket u \rrbracket + h \llbracket U' \rrbracket = 0, \qquad \llbracket v \rrbracket = 0, \tag{22}$$

continuity of stresses,

$$-i\beta h \llbracket N_{1B} \rrbracket + \llbracket T_{12} + i\beta v + u' \rrbracket = 0, \qquad \llbracket T_{22} + 2v' - p \rrbracket = 0, \tag{23}$$

and the kinematic free surface condition

$$(\sigma + i\beta U)h = v. \tag{24}$$

The boundary conditions are no slip at the walls. At $y = 0$ and $y = 1$, the perturbed velocities vanish $u = v = 0$.

This completes the formulation of the eigenvalue problem, symbolically written $L_1[\mathbf{v}] = \sigma L_2[\mathbf{v}]$, where the eigenfunction $\mathbf{v}$ consists of $\{u, v, p, C_{11}, C_{12}, C_{13}$ in layer 1$\}$, $\{u, v, p, C_{11}, C_{12}, C_{13}$ in layer 2$\}$, and h. The linear operators L_1 and L_2 depend on $\{\alpha, \beta, \epsilon, \tau, Re, l_1\}$. The spectrum consists of discrete and continuous parts, which need to be examined for the range of $\alpha > -3$, small Re, small ϵ, and τ such that the steady state shear rate shear stress curve is non-monotone, and for $0 < l_1 < 1$. For each parameter set, the

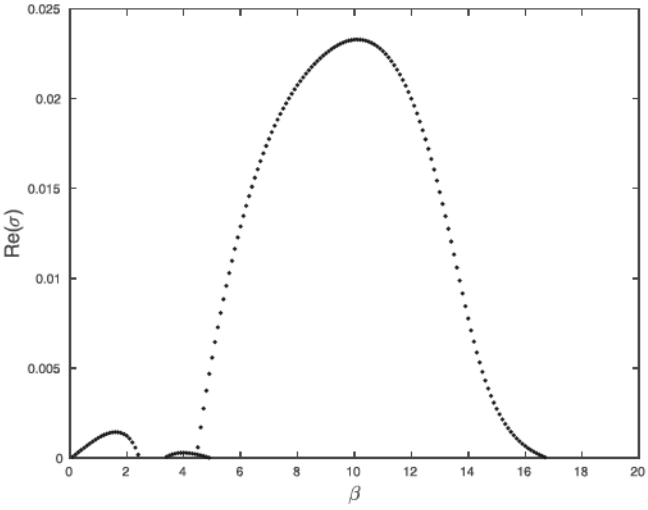

Fig. 19. Growth rate of unstable modes for $\alpha = -1$, $\tau = 0.22$, $l_1 = 0.7$.

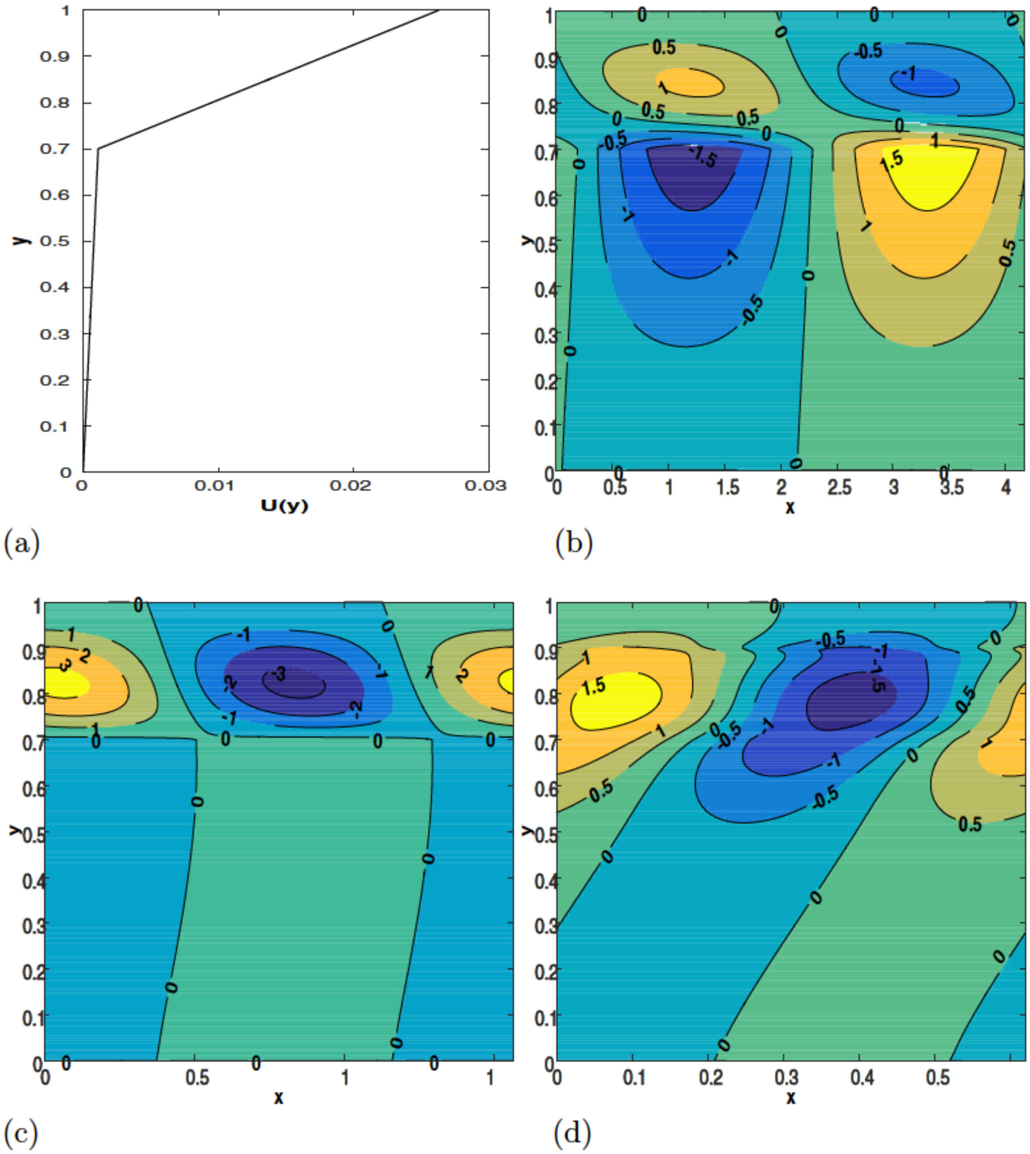

Fig. 20. Stream functions of unstable modes for Fig. 19. (a) base flow profile, (b) $\beta = 1.5$, (c) $\beta = 4$, (d) $\beta = 10.1$. Contour values in units of 10^{-5}.

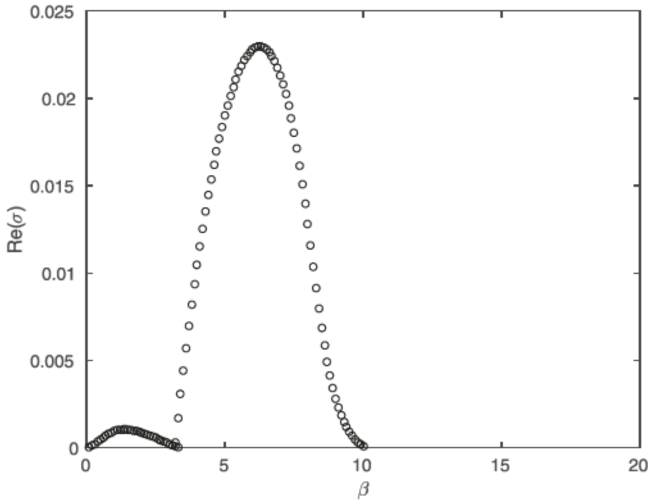

Fig. 21. Growth rate of unstable modes for $\alpha = -1$, $\tau = 0.22$, $l_1 = 0.5$.

spectrum is calculated at all disturbance wavenumbers β. The flow is unstable when there is an eigenvalue σ of positive real part at some values of β.

4. Discrete spectrum in the long wave limit

In the long wave limit, the wavenumber β is zero. The terms that contain $U(y)$ disappear from the linearized equations, which become a system with constant coefficients. In addition, the variables v and C_{22} become zero in this limit. This system is solved in closed form, and finally, a characteristic equation for σ is derived. This characteristic equation is solved analytically, and with Mathematica, and our numerical results agree with the solutions.

5. Continuous spectra

Stability problems in viscoelastic flows always involve continuous spectra. These continuous spectra arise because the equations expressing the constitutive law involve the material time derivative of the stresses but no derivative of stresses across the flow direction. When the differential equations are combined into a single

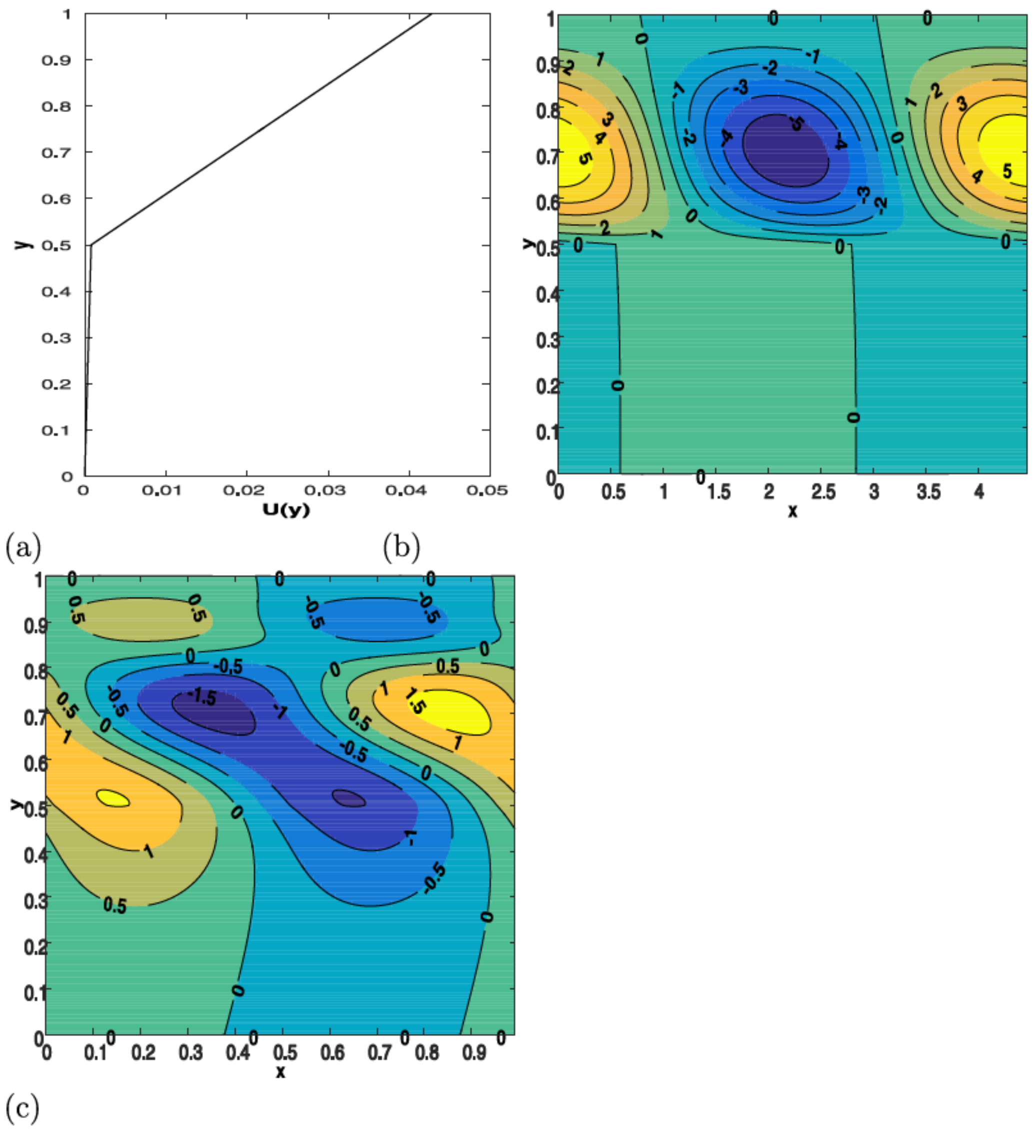

Fig. 22. Stream functions of unstable modes for Fig. 21. (a) base flow profile, (b) $\beta = 1.4$, (c) $\beta = 6.3$. Contour values in units of 10^{-5}.

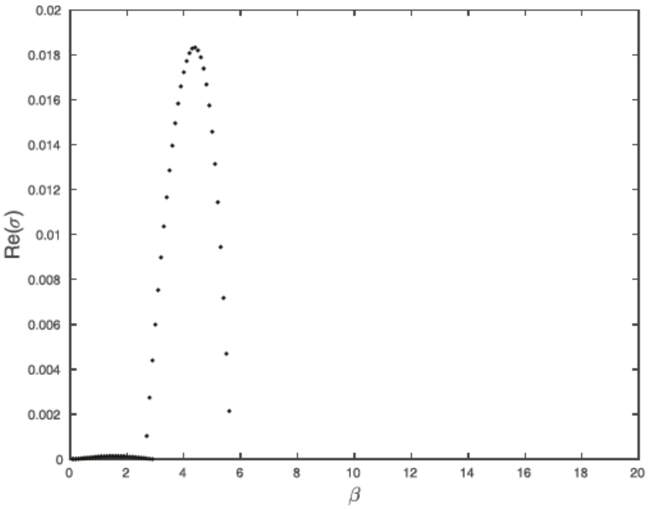

Fig. 23. Growth rate of unstable modes for $\alpha = -1$, $\tau = 0.22$, $l_1 = 0.2$.

equation, there are certain values of σ for which the coefficient of the highest derivative is zero, and these yield the continuous spectrum. We can determine these continuous spectra explicitly, and thereby show that they are stable. These explicit formulas are a useful tool for testing our numerical code that computes the entire spectrum.

We determined the continuous spectra in an analytical calculation performed with Mathematica, and we simply present the result.

For the PECN model, the continuous spectrum is composed of three parts per fluid layer, making a total of six parts. One branch is given by

$$\sigma = -i\beta U(y) - \epsilon(s_B + \alpha). \tag{25}$$

The rest of the continuous spectrum is determined by the quadratic equation

$$b_0(\sigma + i\beta U(y))^2 + b_1(\sigma + i\beta U(y)) + b_2 = 0, \tag{26}$$

where

$$\begin{aligned} b_0 &= -(s_B + \alpha)^2, \\ b_1 &= -3 - \alpha - \epsilon(s_B + \alpha)^2(-3 + 3s_B + 2\alpha), \\ b_2 &= -\epsilon(6 + \alpha - s_B)(\alpha + s_B) - \epsilon^2(\alpha + s_B)^3(-6 + \alpha + 3s_B). \end{aligned} \tag{27}$$

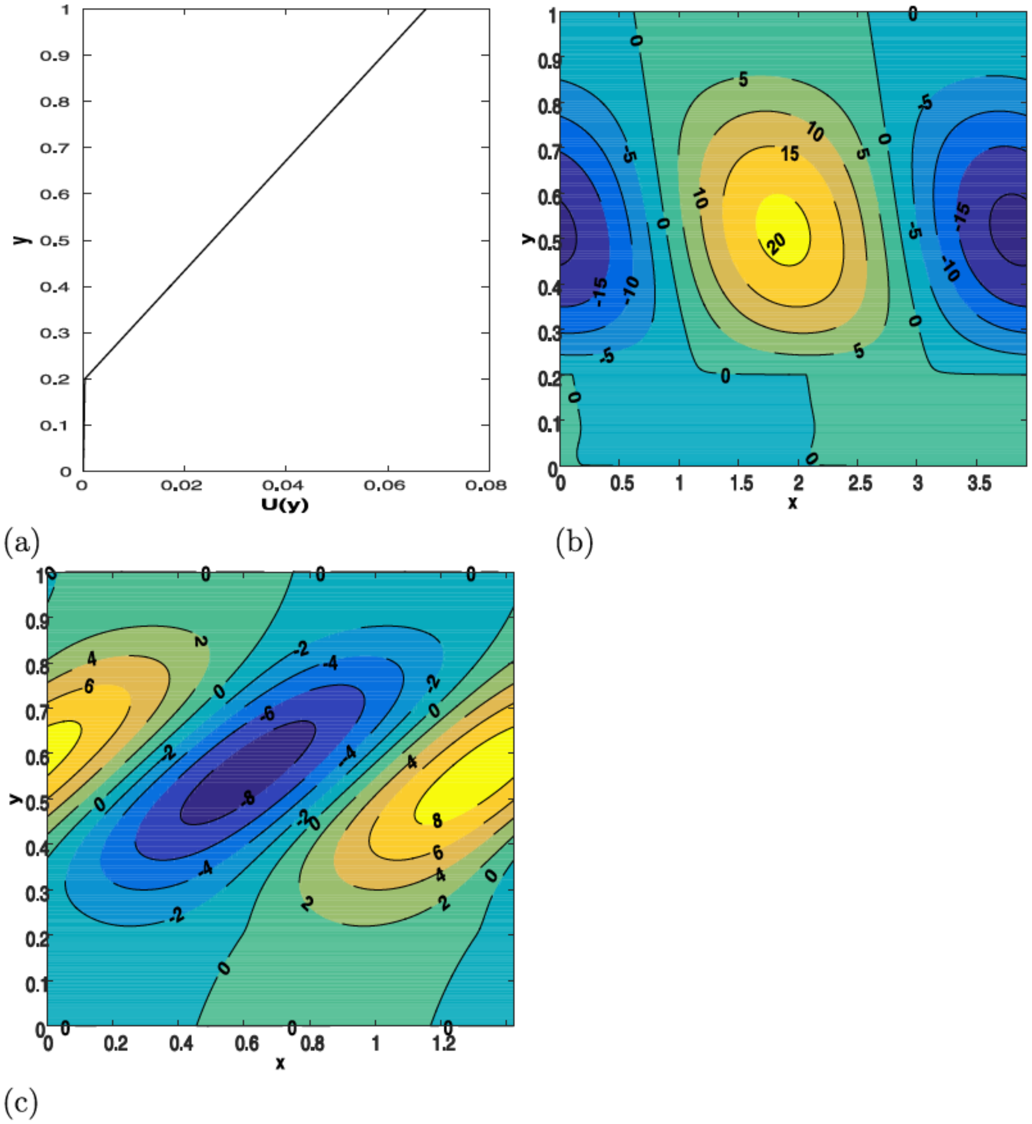

Fig. 24. Stream functions of unstable modes for Fig. 23. (a) base flow profile, (b) $\beta = 1.6$, (c) $\beta = 4.4$. Contour values in units of 10^{-5}.

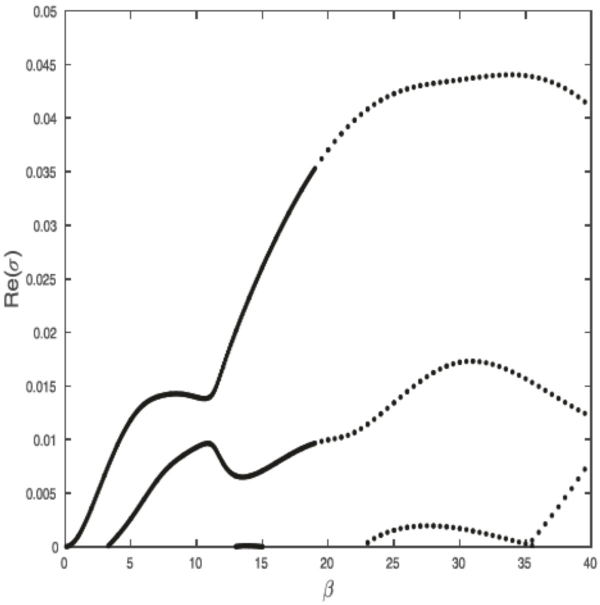

Fig. 25. Growth rate of unstable modes for $\alpha = 5$, $\tau = 0.12$, $l_1 = 0.9$.

For the altered PEC model with $\psi(s) = e^{-s}$, as in (16), the continuous spectrum (25) remains unchanged. In (26), however, we obtain instead the coefficients

$$
\begin{aligned}
b_0 &= \exp(s_B), \\
b_1 &= 4 - s_B + \epsilon \exp(s_B)(-3 + 2\alpha + 3s_B), \\
b_2 &= \epsilon(s_B + \alpha)(7 - 2s_B) + \epsilon^2 \exp(s_B)(s_B + \alpha)(3s_B + \alpha - 6). \quad (28)
\end{aligned}
$$

6. Numerical algorithm

The Chebyshev collocation method [31] is used. The equations are discretized by expanding each perturbation variable within each fluid in a series of Chebyshev polynomials of the first kind, multiplied by the factor $e^{i\beta x + \sigma t}$. For instance, the horizontal velocity in the lower fluid is represented as

$$u_1 = e^{i\beta x + \sigma t} \sum_{n=0}^{n=N-1} a_{1n} T_n(y_1), \quad y = \frac{l_1}{2}(y_1 + 1), -1 < y_1 < 1, \quad (29)$$

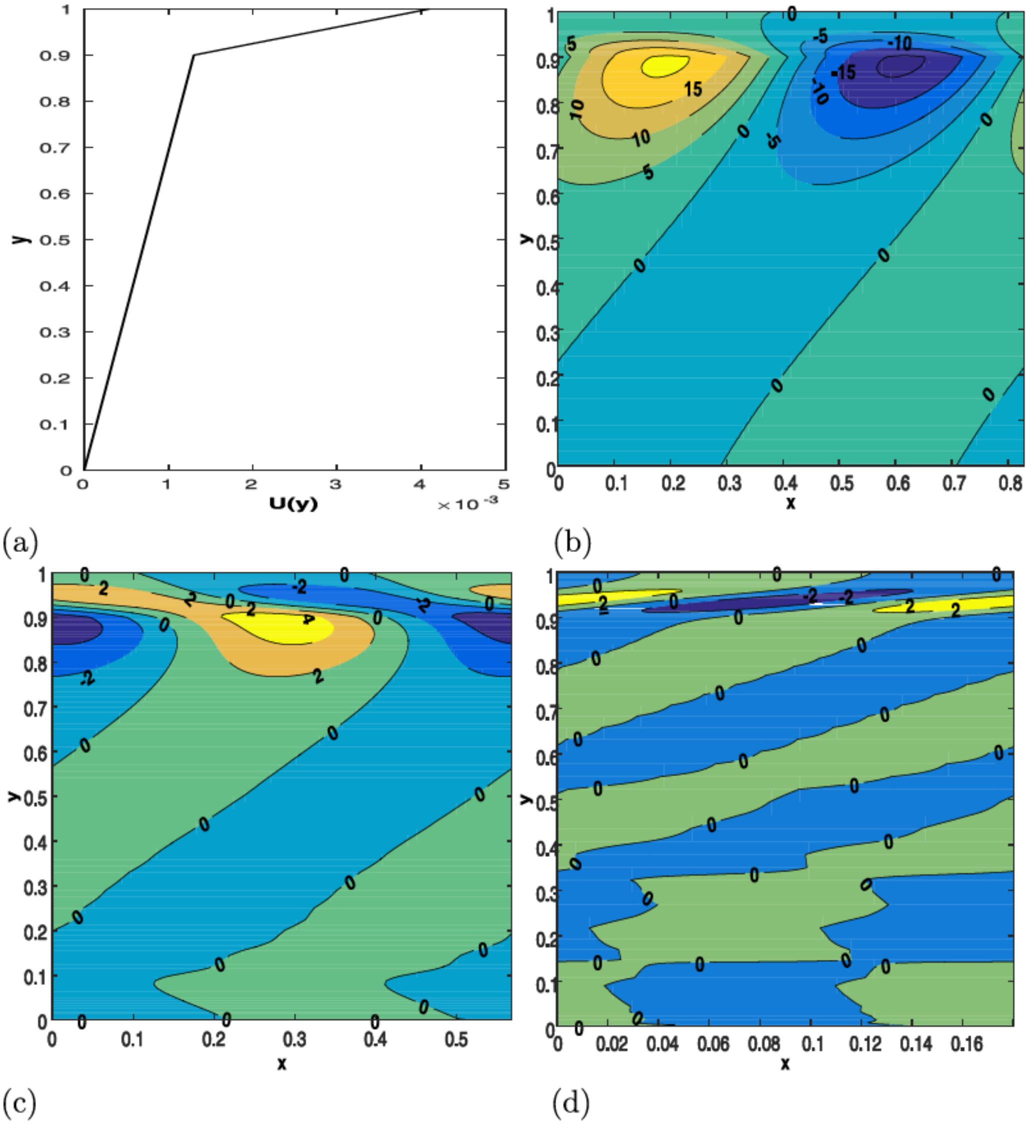

Fig. 26. Stream functions of unstable modes at growth rate maxima in Fig. 25. (a) base flow profile, (b) $\beta = 7.5$, (c) $\beta = 11$, (d) $\beta = 34.5$. Contour values are in units of 10^{-7}.

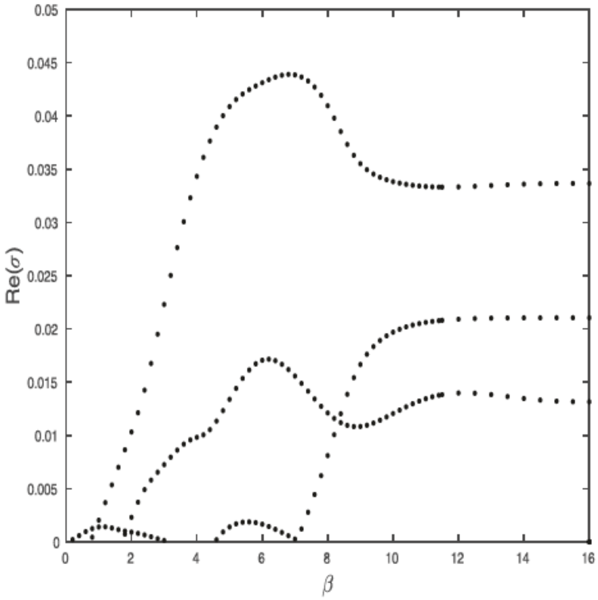

Fig. 27. Growth rate of unstable modes for $\alpha = 5$, $\tau = 0.12$, $l_1 = 0.5$.

and in the upper fluid by

$$u_2 = e^{i\beta x + \sigma t} \sum_{n=0}^{n=N-1} a_{2n} T_n(y_2),$$

$$y = l_1 + \frac{1 - l_1}{2}(y_2 + 1), -1 < y_2 < 1, \quad (30)$$

In each fluid, there are two velocity components, three conformation tensor components and the pressure. Together with the interface position perturbation $he^{i\beta x + \sigma t}$, these constitute the eigenvector of $12N + 1$ unknowns, say **a**. Each equation is evaluated at the N collocation points per layer: y_1 and y_2 at $\cos[k\pi/(N-1)]$, $k = 0, \ldots N-1$. This generates a matrix equation of size $12N + 1$, say $A\mathbf{a} = \sigma B\mathbf{a}$. The boundary and interface conditions are incorporated as follows. The momentum equations require the boundary conditions. Therefore, the first and last rows of the u and v momentum equations in each fluid are replaced by the four boundary conditions and 4 continuity conditions at the interface. Finally, the kinematic condition for h is placed as the last row of equation of the matrix equation.

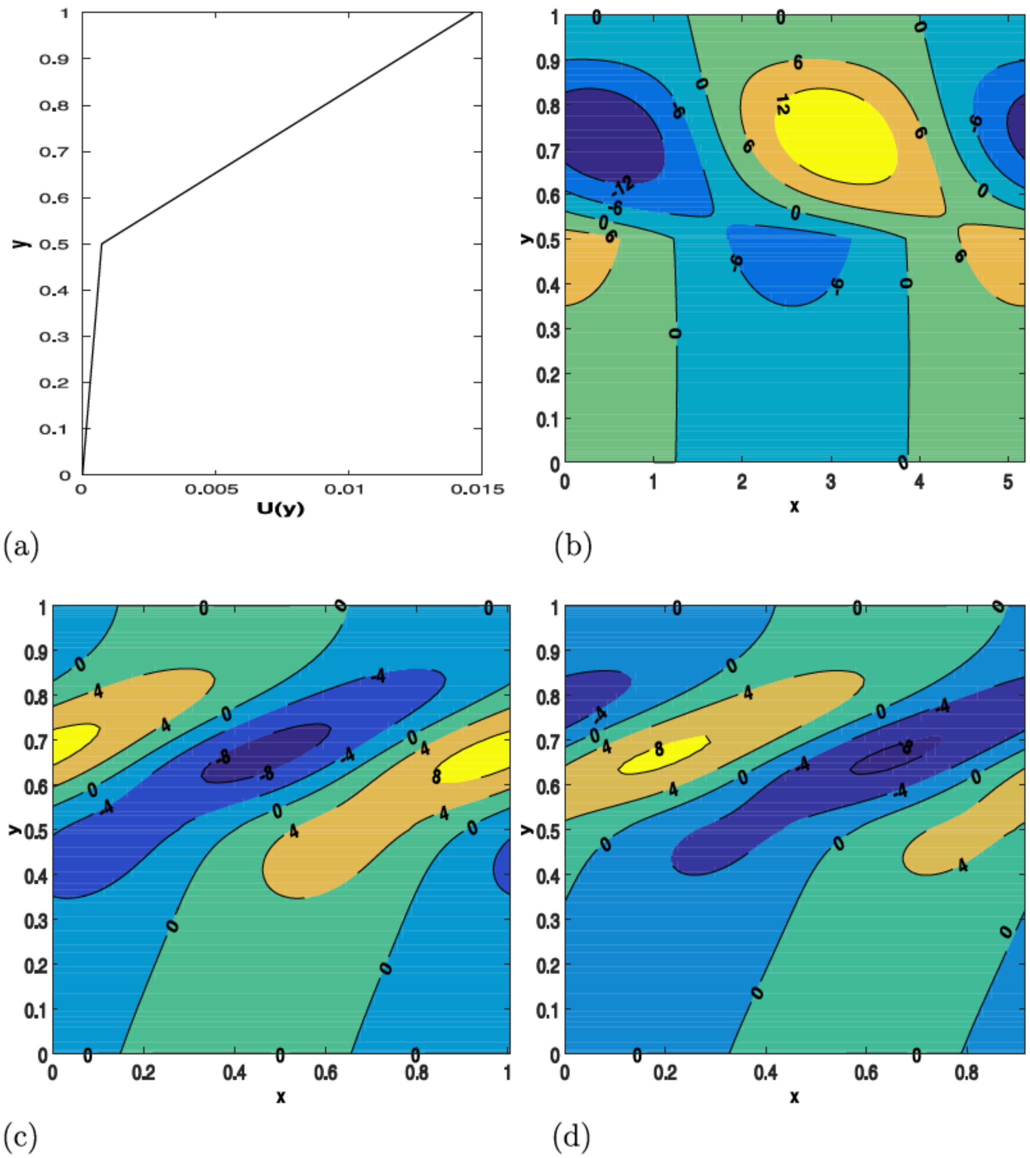

(a) (b) (c) (d)

Fig. 28. Stream functions of unstable modes at growth rate maxima in Fig. 27. (a) base flow profile, (b) $\beta = 1.2$, (c) $\beta = 6.2$, (d) $\beta = 6.8$. Contour values in units of 10^{-6}.

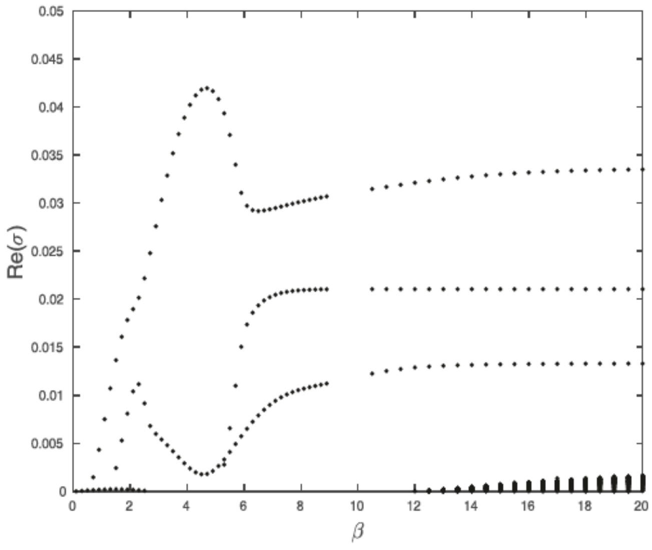

Fig. 29. Growth rate of unstable modes for $\alpha = 5$, $\tau = 0.12$, $l_1 = 0.2$.

Code validation

Our numerical results were checked against the continuous spectra discussed above. For the case of a single fluid phase, we have also checked the consistency for different placements of the artificial “interface.” We also compared numerical results for small β with the asymptotic analysis for the limit $\beta \to 0$.

Some care needs to be taken about the possibility of spurious modes. As an illustrative example, we show a result with $\epsilon = 0.001$, $Re = 0.001$, $\alpha = -1$, $\beta = 2$, $\tau = 0.22$ and $\kappa = 0.084$, $s = 25.85$ in both layers, but with an artificial interface b at $z = l_1 = 0.7$. The computation shows an eigenvalue at approximately $\sigma = -0.03655 - 0.103i$. This eigenvalue converges with increasing N, but is not reproduced when we change l_1. Fig. 3 is a plot of the pressure field for the eigenfunction, which shows rapid oscillations at every discretized point in the yielded phase, clearly revealing its spurious nature. The results reported below are converged not only for the eigenvalues, but also the eigenfunctions.

It is well known that the Chebyshev approximation used in our numerical scheme yields rapid convergence for discrete eigenvalues; the error decreases exponentially with N [32]. On the other

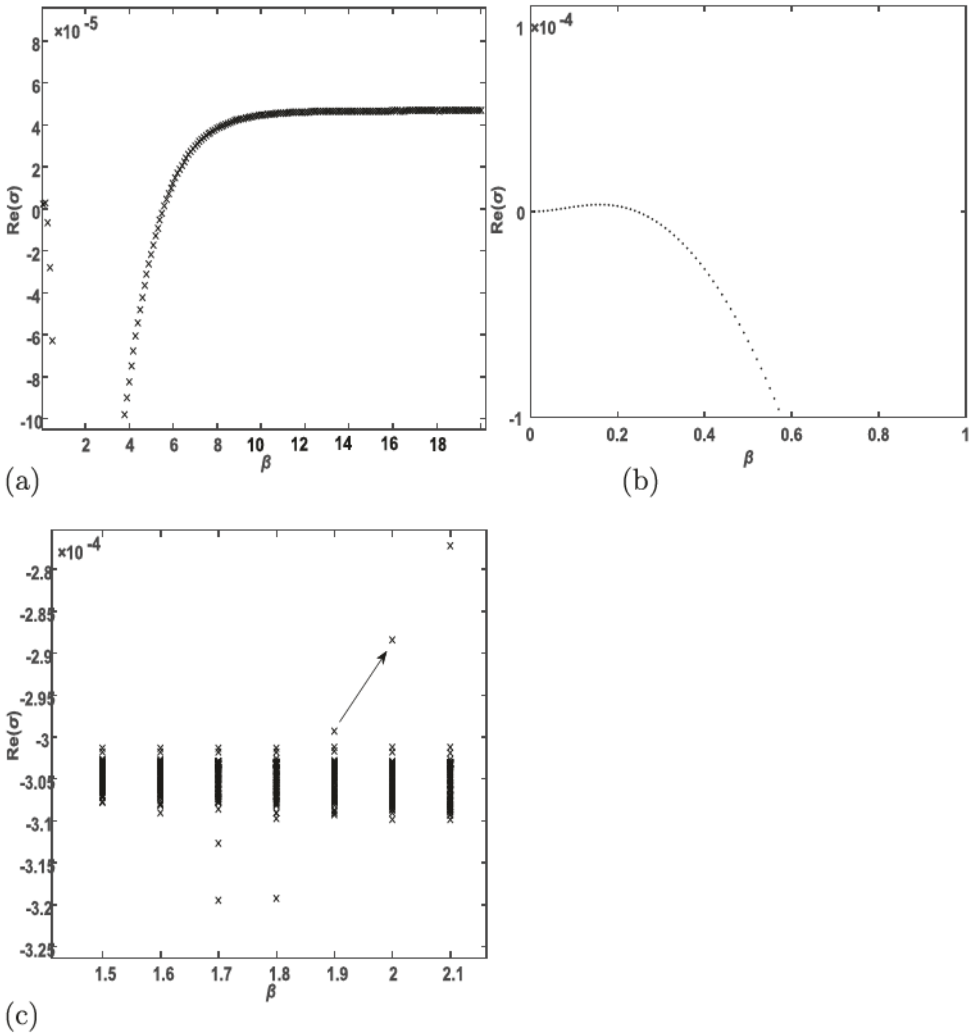

Fig. 30. (a) Growth rate versus β. $Re = 0.001$, $l_1 = 0.7$, $\tau = 0.013$, $\alpha = -2.8$, $\epsilon = 0.001$. The interfacial mode is unstable for long waves. Another mode is unstable for shorter waves. The interval $0.2 < \beta < 5.2$ is stable. (b) Magnification of long wave curve. (c) Emergence of short wave curve from the continuous spectrum.

hand, the approximation of continuous spectra is not well understood theoretically, and all prior experience with viscoelastic fluids shows that they are approximated poorly. This poor approximation of continuous spectra can lead to artificial “instabilities,” especially for large β, and we shall see instances of this below.

7. Numerical results: yielded flow

This section is focussed on the stability of one-fluid flows in the yielded state, at shear rates chosen to correspond to those which will also arise later in shear banded flows. As discussed earlier in Section 2, we focus on small values of Re and ϵ. The numerical results throughout are therefore presented at $Re = 0.001$, and $\epsilon = 0.001$, unless otherwise stated. The effects of varying the following parameters are studied: the ‘yielding parameter’ α, the total shear stress τ, the perturbation wave number β and, for shear banded flow, the interface position l_1.

The values $\alpha = -2.8$, $\alpha = -1$ and $\alpha = 5$ are chosen as a representative set to show the variety of possible behaviors.

For $\alpha = -2.8$, we chose $\tau = 0.65$, $\kappa = 0.5743$. This is in the yielded phase, in the upper part of the range where shearbanding is possible. See Fig. 4 for the shear stress vs. shear rate curve. No instabilities were found for single layer flow.

For $\alpha = -1$, the behavior is exemplified by the shear rate $\kappa = 0.08397$, and shear stress $\tau = 0.22$, which also corresponds to the yielded phase, in a range where shearbanding can occur. The constitutive curve for this case is shown in Fig. 1. We find an unstable mode roughly in the range $2.6 \le \beta \le 4.4$. The eigenvalue corresponding to this mode emerges from the continuous spectrum roughly at $\beta = 1.8$, then goes unstable near $\beta = 2.6$. For $\beta > 4.5$, the eigenvalue becomes stable again and eventually merges back into the continuous spectrum. Fig. 5 shows the growth rate as a function of β and the perturbation stream function for $\beta = 3.6$, which is roughly where maximum growth occurs. The stream functions at other values of β look similar. The flow pattern is symmetric, with stream line contours slanted in the direction of the shear. Fig. 6 shows the overall spectrum at $\beta = 3.6$. We see the single unstable eigenvalue in the right half plane and the lines representing the continuous spectrum in the left half plane, as well as a number of other (stable) discrete modes, some of which are spurious. The continuous spectrum consists of three lines, the one in the middle corresponds to (25) and the outer ones to (26).

For $\alpha = 5$, the dependence of shear stress on shear rate is monotone at $\epsilon = 0.001$, so we chose $\epsilon = 0.0001$ instead. The behavior of unstable modes is exemplified by the parameters $\tau = 0.12$ and $\kappa = 0.0422$. We show the constitutive curve in Fig. 7.

We find several unstable modes, and a number of instances where two modes merge and form a pair.

Fig. 8 shows the growth rates of unstable modes as a function of β. The figure appears to show a cluster of eigenvalues with small growth rate for $\beta > 5$. These actually result from poor approximation of the stable continuous spectrum. The discrete modes shown in the figure are converged. Fig. 9 shows the full spectrum for $\beta = 5$. We see four unstable discrete eigenvalues. The continuous spectrum, which should be a vertical line, bulges out towards the right and will cross the axis for larger values of β. This part of the continuous spectrum is the more unstable one corresponding to (26); the second line comes from (25). The second line corresponding to (26) is further to the left, outside the window of the plot. As the number of modes is increased, approximation of the continuous spectrum slowly improves. In general, we find that $N = 20$ or 30 is enough to capture the most unstable discrete modes, for modes of very low growth rate higher values are needed, on the order of 200 or 300.

For $\beta = 1.5$, there are two unstable modes. Their streamfunctions are shown in Fig. 10. Plot (a) shows the mode with the higher growth rate, and plot (b) shows the mode with the lower growth rate. Both modes are symmetric about the centerline. The mode shown in plot (b) shows contours inclined in the direction of the shear, while the mode in plot (a) shows no such inclination.

Fig. 11 shows the stream function for the most unstable mode at $\beta = 4$. The streamline pattern is similar to the mode with the lower growth rate at $\beta = 1.5$. Indeed, the growthrate plot in Fig. 8 shows that the two modes which are unstable at $\beta = 1.5$ essentially cross over near $\beta = 2$, with a small interval where they form a pair. So it is natural to think of the more unstable mode at $\beta = 4$ as a continuation of the less unstable mode at $\beta = 1.5$.

Fig. 8 shows several instances where two unstable eigenvalues merge and form a pair. For instance, there is such an occurrence for β just above 5. The result of such pairings are asymmetric modes. We show the stream function for one of the pair of most unstable modes at $\beta = 7$ in Fig. 12; the other mode is symmetric to it.

8. Numerical results: shear banded flow

In this section, we show stability results for shear banded flow, with the same parameters for α and τ which we used above for single layer yielded flow.

We begin with $\alpha = -2.8$, $\tau = 0.65$. For this case, we found no bulk instabilities in the preceding section. For the two-layer case, we investigate three different interface positions: $l_1 = 0.7$, $l_1 = 0.5$ and $l_1 = 0.2$. Fig. 13 shows the growth rate of an interfacial mode. The instability shifts to longer wavelengths as l_1 is decreased. This would be expected, since the same ratio of perturbation wave length to the depth of the yielded fluid is reached at a smaller β. The maximum growth rate is roughly at $\beta = 5.6$ for $l_1 = 0.7$. For $l_1 = 0.5$, there are two maxima, at 0.5 and 2.7. For $l_1 = 0.2$, maximum growth is at $\beta = 1.8$.

Figs. 14–16 show stream functions of the interfacial mode at the growth rate maxima in Fig. 13. Part (d) of Fig. 15 shows the stream function for $l_1 = 0.5$ and $\beta = 20$, which is in the range where the mode is stable. It illustrates the interfacial character of the mode, showing localization at the interface.

For $\alpha = -1$, $\tau = 0.22$, we investigate four different depth ratios between the unyielded and yielded phases: $l_1 = 0.9$, $l_1 = 0.7$, $l_1 = 0.5$ and $l_1 = 0.2$. Fig. 17 shows the growth rates of unstable modes for $l_1 = 0.9$. There is a long wave instability for β less than about 10. This is an interfacial mode. Then there are two unstable modes for higher β, which correspond to the bulk modes in the single fluid case. Fig. 18 shows the stream function of each mode, roughly at that value of β which corresponds to its maximum growth rate. Figs. 19 and 20 show the analogous information for $l_1 = 0.7$. As the width of the yielded layer increases, the instability shifts to longer wave length. For the other two depth ratios, we find an interfacial long wave mode and one unstable bulk mode at shorter wave lengths. The growth rates and stream functions are shown in Figs. 21–24.

The long wave modes are "interfacial" in the sense that they connect to the neutrally stable interfacial mode at $\beta = 0$. The streamline pattern is more suggestive of an interface mode when the yielded fluid is in a thin layer, see Fig. 18 (a) and 20 (a). For smaller values of l_1, even this mode shows a streamline pattern dominated by circulation in the yielded phase. The growthrate of the long wave becomes much smaller as the width of the yielded layer is increased. The other modes are essentially bulk modes. In terms of growth rates, one of these is dominant.

We now turn to the case $\alpha = 5$, $\tau = 0.12$; the corresponding stability problem for the single layer yielded flow is analyzed in the previous section. We investigate three positions of the interface: $l_1 = 0.9$, $l_1 = 0.5$ and $l_1 = 0.2$. Fig. 25 shows the growth rate of unstable modes for $l_1 = 0.9$. One of these is a long wave mode which connects to the neutrally stable interfacial eigenvalue at $\beta = 0$. A new feature in this plot is that the modes seems to remain unstable for large β; this is not observed in the single layer case. Fig. 26 shows streamline plots of the unstable mode at the growth rate maxima at $\beta = 7.5$ and $\beta = 34.5$ (uppermost curve in Fig. 25) and $\beta = 11$ (second curve from the top in Fig. 25). The maxima at 7.5 and 34.5 are on the same curve. The visual picture of the stream function at $\beta = 7.5$ still suggests an interfacial mode, while the picture at $\beta = 34.5$ looks more like a bulk mode in the yielded phase. This is also reflected in the wave speeds of the unstable mode. For the parameters chosen, the fluid speed at the interface is 0.00156, and the base flow speed in the middle of the yielded layers is 0.00367. The mode at $\beta = 7.5$ has a wave speed of 0.00279, at $\beta = 34.5$ it is 0.00309. So for higher β, the wave speed shifts closer to the fluid speed in the center of the yielded layer, and the mode becomes more like a bulk mode.

Figs. 27 and 28 show growth rates and stream function plots for $l_1 = 0.5$. As we saw above for $\alpha = -1$, the maximum growth rate shifts to lower waves numbers as l_1 is decreased. The base flow speed at the interface for this case is 0.00086, and the bases flow speed in the middle of the yielded layer is 0.0114. The wave speeds of the unstable modes are 0.00225 at $\beta = 1.2$, 0.0085 at $\beta = 6.2$ and 0.0086 at $\beta = 6.8$. Again, the character of the unstable mode becomes more like that of a bulk mode as β is increased. Fig. 29 shows the growth rate for $l_1 = 0.2$. The overall pattern is similar to the previous cases. The cluster near the axis which emerges for $\beta > 12$ is from poor approximation of the continuous spectrum and should be ignored.

9. A more strongly shear thinning model

For both the PEC and Johnson–Segalman fluid, the first normal stress difference is larger in the yielded phase than in the unyielded phase. It is natural to ask whether this is crucial for creating instability of shear banded flow, since the normal stress jump enters the interface conditions and plays a crucial role in driving the instability. For this reason, we investigate a model with a structure similar to PEC, but with a lower normal stress in the yielded phase. This model is given at the end of Section 2 by Eqs. (16) and (17). We find no instabilities for the case of a single layer in this model. However, there are instabilities in shear banded flow. Fig. 30 shows growth rates computed for $l_1 = 0.7$, $\tau = 0.013$, $\alpha = -2.8$, $\epsilon = 0.001$. Fig. 2 shows the steady state constitutive behavior for these parameters. We find instabilities for short waves, $\beta > 5.2$. There is also a narrow range of wave numbers for long waves, with very small growth rates. The instability is interfacial; the long wave mode connects to the neutrally stable mode at $\beta = 0$, and for the short wave mode, the Im σ is

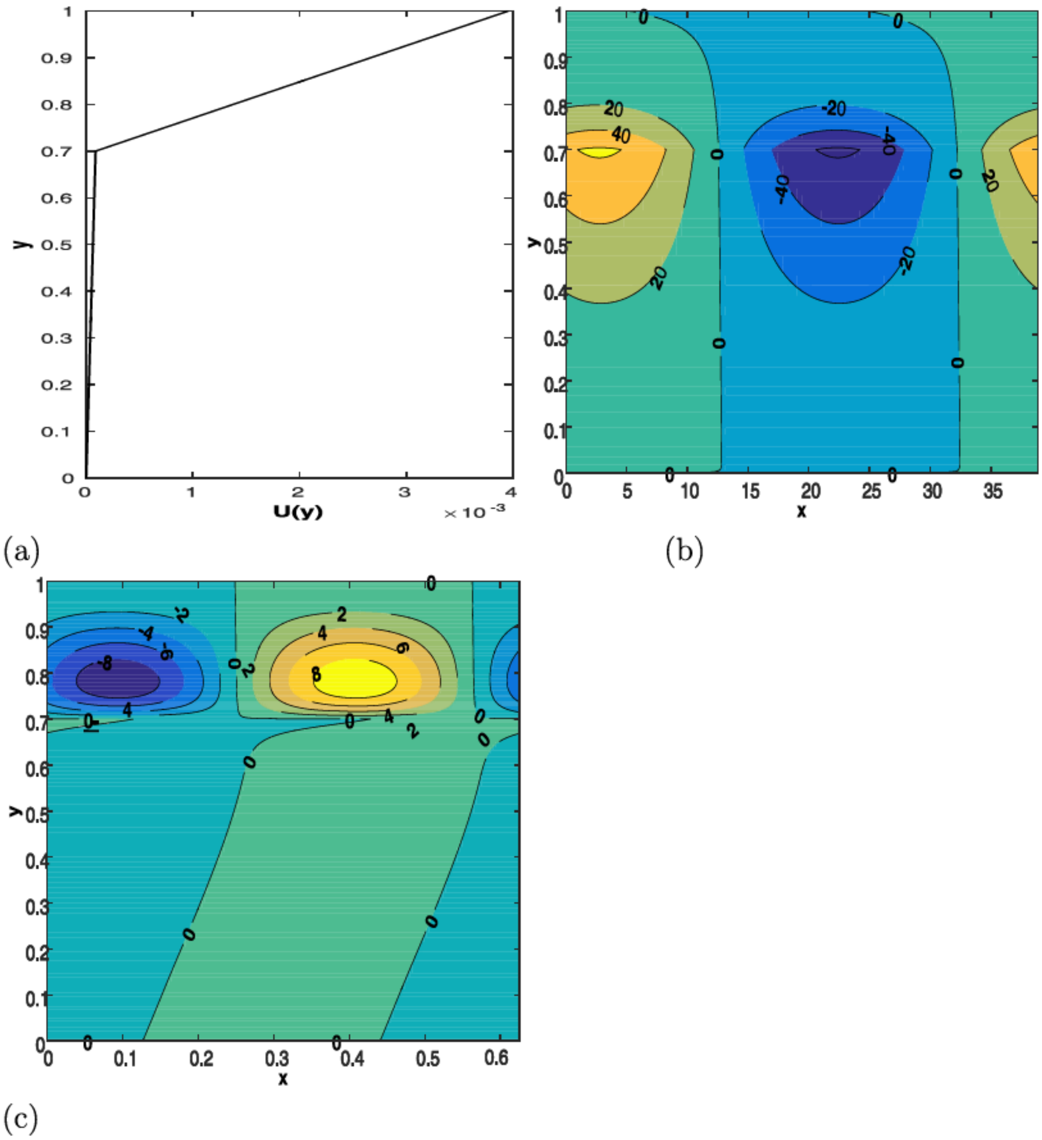

(a)

(b)

(c)

Fig. 31. Stream functions for unstable modes shown in Fig. 30. (a) base flow profile, (b) $\beta = 0.16$, (c) $\beta = 10$. Contour values in units of 10^{-6}.

roughly $-i\beta U(l_1)$. The short wave curve does not connect to the long wave curve, but emerges from the continuous spectrum at a finite value of β; this is demonstrated in part (c) of Fig. 30. Fig. 31 shows stream functions for the long and short wave modes.

10. Conclusions

We have investigated the linear stability of shear banded flows for the PECN model. We investigated three representative cases: $\alpha = -2.8$, $\alpha = -1$ and $\alpha = 5$. The model parameter α is related to the ratio of the yield stress to the stress modulus, which is given by $\sqrt{\alpha + 3}/2$. For $\alpha = -1$ and $\alpha = 5$, we found bulk instabilities in the yielded phase. These bulk instabilities become the dominant mechanism of instability in shear banded flows, but interfacial long wave instabilities are also present. Bulk instabilities are absent for $\alpha = -2.8$, but there are interfacial long wave instabilities. We also investigated a more strongly shear thinning model in which the first normal stress difference in the yielded phase is smaller than that in the unyielded phase, in contrast to both the PEC and Johnson–Segalman models. For this model, we found no bulk instabilities, but there are interfacial instabilities for both long and short wave modes.

All the cases of shearbanded flows that we investigated show instabilities. However, due to the presence of both interfacial and bulk instabilities, the final picture is quite varied and depends on the model in ways that are far from obvious.

Acknowledgments

This research is supported in part by NSF-DMS 1311707 and NSF-DMS 1514576.

References

[1] H.A. Barnes, K. Walters, The yield stress myth? Rheol. Acta 24 (1985) 323–326.
[2] M. Cates, S. Fielding, Rheology of giant micelles, Adv. Phys. 55 (2006) 799–879.
[3] T. Divoux, M.A. Fardin, S. Manneville, S. Lerouge, Shear banding of complex fluids, Ann. Rev. Fluid Mech. 48 (2016) 81–103.
[4] S.M. Fielding, Shear banding in soft glassy materials, Rep. Progr. Phys. 77 (2014) 102601.
[5] P.C.F. Møller, S. Rodts, M.A.J. Michels, D. Bonn, Shear banding and yield stress in soft glassy materials, Phys. Rev. E 77 (2008) 041507.
[6] N. Spenley, X. Yuan, M. Cates, Nonmonotonic constitutive laws and the formation of shear-banded flows, J. Physique II 6 (1996) 551–571.
[7] M. Renardy, The mathematics of myth: yield stress behavior as a limit of non-monotone constitutive theories, J. Non-Newtonian Fluid Mech. 165 (2010) 519–526.

[8] H.A. Barnes, The yield stress - a review -everything flows? J. Non-Newtonian Fluid Mech. 81 (1999) 133–178.

[9] K.L. Maki, Y. Renardy, The dynamics of a viscoelastic fluid which displays thixotropic yield stress behavior, J. Non-Newtonian Fluid Mech. 181-182 (2012) 30–50.

[10] Y. Renardy, Stability of the interface in two-layer Couette flow of upper convected maxwell liquids, J. Non-Newtonian Fluid Mech. 28 (1988) 99–115.

[11] K. Chen, Interfacial instability due to elastic stratification in concentric coextrusion of two viscoelastic fluids, J. Non-Newtonian Fluid Mech. 40 (1991) 155–175.

[12] Y. Renardy, Spurt and instability in a two-layer Johnson–Segalman liquid, Theor. and Comp. Fluid Dyn. 7 (1995) 463–475.

[13] S.M. Fielding, Linear instability of planar shear banded flow, Phys. Rev. Lett. 95 (2005) 134501.

[14] S.M. Fielding, Complex dynamics of shear banded flows, Soft Matter 3 (2007) 1262–1279.

[15] H.J. Wilson, S.M. Fielding, Linear instability of planar shear banded flow of both diffusive and non-diffusive Johnson–Segalman fluids, J. Non-Newtonian Fluid Mech. 138(2-3) (2006) 181–196.

[16] T. McLeish, Stability of the interface between two dynamic phases in capillary flow of linear polymer melts, J. Polym. Sci. B 25 (1987) 2253–2264.

[17] S. Fielding, P. Olmsted, Nonlinear dynamics of an interface between shear bands, Phys. Rev. Lett. 96 (2006) 104502.

[18] S. Fielding, H. Wilson, Shear banding and interfacial instability in planar poiseuille flow, J. Non-Newtonian Fluid Mech. 165 (2010) 196–202.

[19] A. Nicholas, A. Morozov, Nonaxisymmetric instability of shear-banded taylor–couette flow, Phys. Rev. Lett. 108 (2012) 088302.

[20] R.G. Larson, A constitutive equation for polymer melts based on partially extending strand convection, J. Rheol. 28 (1984) 545–571.

[21] L. Zhou, P.A. Vasquez, L.P. Cook, G.H. McKinley, Modeling the inhomogeneous response and formation of shear bands in steady and transient flows of entangled liquids, J. Rheol. 52 (2008) 591–623.

[22] P. Nghe, S. Fielding, P. Tabeling, A. Ajdari, Interfacially driven instability in the microchannel flow of a shear-banding fluid, Phys. Rev. Lett. 104 (2010) 248303.

[23] P. Decruppe, L. Bécu, O. Greffier, N. Fazel, Azimuthal instability of the interface in a shear banded flow by direct visual observation, Phys. Rev. Lett. 105 (2010) 258301.

[24] M. Cromer, L.P. Cook, G.H. McKinley, Interfacial instability of pressure-driven channel flow for a two-species model of entangled wormlike micellar solutions, J. Non-Newtonian Fluid Mech. 166 (2011) 566–577.

[25] H. Wilson, J. Rallison, Instability of channel flow of a shear-thinning white-metzner fluid, J. Non-Newtonian Fluid Mech. 87 (1999) 75–96.

[26] H. Wilson, V. Loridan, Linear instability of a highly shear thinning fluid in channel flow, J. Non-Newtonian Fluid Mech. 223 (2015) 200–208.

[27] C. Pipe, N. Kim, P. Vasquez, L. Cook, G. McKinley, Wormlike micellar solutions: Ii. comparison between experimental data and scission model predictions, J. Rheol. 54 (2010) 881–913.

[28] M. Cromer, L. Cook, G. McKinley, Pressure-driven flow of wormlike micellar solutions in rectilinear microchannels, J. Non-Newtonian Fluid Mech. 166 (2011) 180–193.

[29] C.-Y. Lu, P. Olmsted, R. Ball, Effects of non-local stress on the determination of shear banding flow, Phys. Rev. Lett. 84 (2000) 642–645.

[30] O. Radulescu, P. Olmsted, J. Decruppe, S. Lerouge, J.-F. Berret, G. Porte, Time scales in shear banding of wormlike micelles, Europhys. Lett. 62 (2003) 230.

[31] S. Orszag, Accurate solutions of the orr-sommerfeld stability equation, J. Fluid Mech. 50 (1971) 689–703.

[32] D. Gottlieb, S. Orszag, Numerical Analysis of Spectral Methods, CBMS-NSF Regional Conference Series in Applied Mathematics, Vol. 26, SIAM Philadelphia, 1977.